STARS

2011

Infrared Phased-array Antenna-coupled Tunnel Diodes

Brian Alan Slovick
University of Central Florida

Showcase of Text, Archives, Research & Scholarship

INFRARED PHASED-ARRAY
ANTENNA-COUPLED TUNNEL DIODES

by

BRIAN ALAN SLOVICK
B.S. San Diego State University, 2005
M.S. San Diego State University, 2007

A dissertation submitted in partial fulfillment of the requirement
for the degree of Doctor of Philosophy
in the College of Optics and Photonics: CREOL & FPCE
at the University of Central Florida
Orlando, Florida

Spring Term
2011

Major Professor: Glenn D. Boreman

ABSTRACT

Infrared (IR) dipole antenna-coupled metal-oxide-metal (MOM) tunnel diodes provide a unique detection mechanism that allows for determination of the polarization and wavelength of an optical field. By integrating the MOM diode into a phased-array antenna, the angle of arrival and degree of coherence of received IR radiation can be determined.

The angular response characteristics of IR dipole antennas are determined by boundary conditions imposed by the surrounding dielectric or conductive environment on the radiated fields. To explore the influence of the substrate configuration, single dipole antennas are fabricated on both planar and hemispherical lens substrates. Measurements demonstrate that the angular response can be tailored by the thickness of the electrical isolation stand-off layer on which the detector is fabricated and/or the inclusion of a ground plane.

Directional detection of IR radiation is achieved with a pair of dipole antennas coupled to a MOM diode through a coplanar strip transmission line. The direction of maximum angular response is altered by varying the position of the diode along the transmission line connecting the antenna elements. By fabricating the devices on a quarter wave layer above a ground plane, narrow beam widths of 35° full width at half maximum and reception angles of ± 50° are achievable with minimal side-lobe contributions. Phased-array antennas can also be used to assess the degree of coherence of a partially coherent field. For a two-element array, the degree of coherence is a measure of the correlation of electric fields received by the antennas as a function of the element separation.

To Dana, Mark, Mom, and Dad

ACKNOWLEDGEMENTS

I would like to thank Dr. Glenn Boreman for his invaluable support. As my mentor, he has enabled both my professional and personal growth.

I would like to acknowledge Dr. Jerry Krassner at Integrity Applications Inc. for funding my research with prototype optical phased-array antennas.

I would like to thank the members of my committee, including Dr. James Harvey, Dr. Winston Schoenfeld, and Dr. Brian Lail for their support of my dissertation work.

I also wish to thank several present and former members of the IR Systems lab for their support during my three and a half years at CREOL, including Dr. Peter Krenz and Dr. Jeffrey Bean, who taught me everything I know about nanofabrication, Guy Zummo for his instruction and contributions to my research, Dr. Jeff Tharp, Dr. James Ginn, Dr. Dave Shelton, Wilson Caba, Lou Florence, Larry Schneider, Sam Wadsworth, Alex Dillard, Jeff Darchangel, Robert Brown, Bill Franklin, and Dan Mullally. I would also like to thank Dr. Ivan Divliansky for his technical assistance with the Leica electron-beam lithography tool.

Most importantly, I want to thank my close friends and family, including my brother Mark and his wife Francie, my Mom for instilling the importance of education, my Dad and his wife Lillian, and Peter. And finally, I want to thank my beautiful and intelligent girlfriend Dana for her love and support.

TABLE OF CONTENTS

LIST OF FIGURES

CHAPTER 1: ANTENNA-COUPLED MOM DIODES

Infrared (IR) detectors can be divided into three general categories: photonic or quantum detectors, thermal detectors, and radiation field detectors. Photonic detectors come in several varieties, including photovoltaic, photoconductive, and photoemissive types [1]. The photovoltaic effect is caused by the diffusion of electrons and holes across a p-n junction under a photon flux. When the incident photon energy exceeds the built-in voltage of the depletion region, electrons diffuse from the p to the n region while holes diffuse from the n to the p region. This process leads to an enhanced electric field in the depletion region and thus to the generation of electrical current in an external circuit. The current-voltage (*I-V*) characteristic of a p-n junction is nonlinear, enabling rectification or directionality of current flow.

Photoconductive detectors operate on the basis of a change in conductivity of a semiconductor under a photon flux. If the photon energy exceeds the energy difference between the valence and conduction bands in the semiconductor, additional electrons are excited into the conduction band, leading to additional charge carriers and thus increased conductivity. By applying a constant bias voltage across the photoconductor, changes in electrical conductivity lead to variations in the electrical current in proportion to the incident irradiance. Photoemissive detectors operate via the photoelectric effect, i.e. the generation of free electrons by radiation with energy exceeding the binding energy of electrons in a semiconductor or metal.

Bolometers are thermal detectors which rely on a change in electrical resistance when radiation is absorbed by a bolometer and converted to heat [1]. In contrast with photodetectors, the spectral response of a bolometer is uniform and depends only on the incident energy. Under

an applied constant current, one measures a change in voltage corresponding to a variation in optical power. In this context, the sensitivity of a bolometer is determined by its temperature coefficient of resistance (TCR). Increased sensitivity can be achieved by cooling the bolometer so that small changes in temperature represent large percentage changes in resistance.

Other thermal detection mechanisms include the thermocouple and pyroelectric effect. A thermocouple utilizes the change in voltage that accompanies a temperature gradient across a junction between dissimilar conductors. One can form a thermopile by connecting several thermocouples in series. Finally, pyroelectric detectors rely on a change in electrical polarization of the material in a capacitor. A change in electrical polarization, or dielectric constant, leads to a change in capacitance and thus a change in charge stored across the capacitor. This, in turn, is accompanied by a change in voltage in the external circuit.

Radiation field detectors respond to changes in the electromagnetic field. Typically, field detectors utilize a coupling element to receive and transfer electromagnetic energy to a sub-wavelength detector. In this configuration, the coupling element can be tailored to achieve the desired polarization and spectral response. However, the detector must be electromagnetically distinguishable from the coupling structure. For example, if the TCR of an antenna-coupled micobolometer is not several orders of magnitude greater than the antenna and lead-lines, the measured response will receive contributions from both, and a careful calibration procedure is required to extract the desired antenna response [2]. To address these issues, we replace the microbolometer with a metal-oxide-metal (MOM) tunnel diode [3, 4]. MOM diodes exhibit high IR impedance and a non-linear current-voltage (*I-V*) characteristic, and thus are capable of rectifying high-frequency antenna currents. Since the tunneling current originates at a localized

area on the antenna, the diode can be regarded as a point detector. Operation of such devices has been extended to the long wave infrared band with promising results [5]. In addition to its capability to operate as a point detector, MOM diodes offer several advantages beyond conventional IR detectors, including functionality without a bias voltage, operation at room temperature without cooling, and CMOS-compatible fabrication.

For certain applications, it may be desirable to alter the angular response pattern of the antenna, including the beam width or angular resolution and the angle of maximum response. We'll find that this can be accomplished in several ways. For a single dipole antenna, the angular response can be tailored by altering the substrate configuration on which the antenna is fabricated. Alternatively, if the detector is integrated with a phased-array antenna, the angular response is determined by the number of antenna elements, the separation of the elements, and the location of the detector relative to the antennas.

1.1 Field-Assisted Tunneling

The metal-oxide-metal tunnel diode can be regarded as a parallel plate capacitor with a nonlinear resistance. The current-voltage characteristics of the MOM diode can be determined from the energy band diagram of the metal-insulator-metal structure shown in Figure 1 [6]. Consider an asymmetric structure comprised of two different metals with work functions Φ_1 and Φ_2 and an insulator barrier of thickness d. Each metal-insulator interface can be assigned a potential barrier height ϕ_i that is by definition the difference between the conduction band of the oxide and the work functions of the metals.

Since the former is not a well defined quantity, the barrier heights are not readily calculable from the metal work functions. Instead, one might interpret the insulator conduction band as the breakdown energy of the dielectric. Later, we'll find that the rectified current produced by the diode is proportional to the difference between the barrier heights, and thus to the difference between the metal work functions.
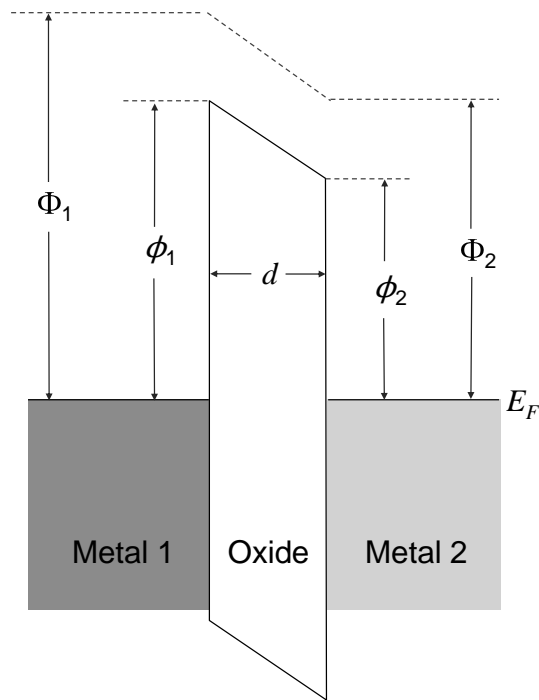
Figure 1: MOM diode energy band diagram.

When the metals are brought into contact with the oxide layer, the system tends towards thermal equilibrium through diffusion until the Fermi energy levels of the two metals align. This gives rise to a built-in field in the oxide barrier without applied bias. Infrared radiation can be regarded time varying optical voltage [7],

$$V(t) = V_b + V_0 \cos(2\pi f t), \tag{1}$$

where V_b is the bias voltage, V_0 is the amplitude of the induced voltage, and f is the frequency of the infrared radiation. With a forward bias, the optical voltage has the same polarity as the barrier height difference, resulting in an enhanced electric field in the oxide layer, as shown in Figure 2. As a result, the probability for electrons to tunnel through the oxide layer increases.

Under reverse bias, the electric field in the oxide is diminished and the electron tunneling probability decreases. Therefore, an asymmetric MOM diode promotes current flow in one direction. This field-assisted tunneling mechanism gives rise to nonlinearities in the *I-V* characteristic which allow the generation of rectified IR currents without applied bias.
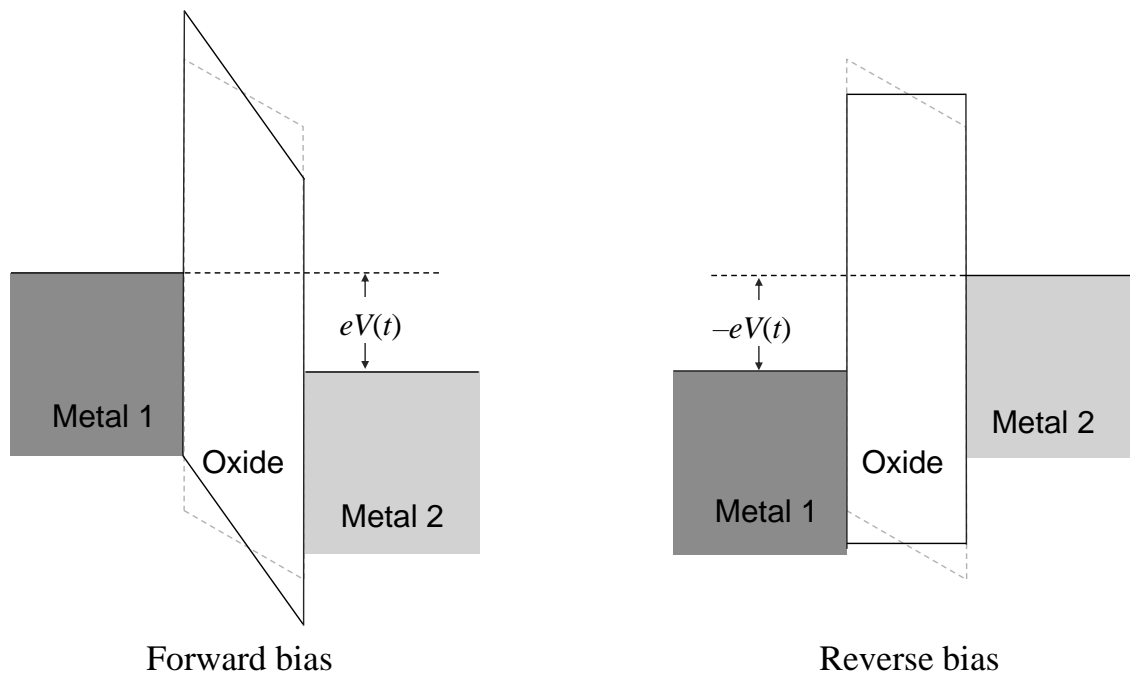
Figure 2: Field-assisted tunneling in a MOM diode.

In order to achieve rectification at IR frequencies, the MOM diode must be connected to an IR ac voltage source. One possibility is to couple the MOM diode to a half-wavelength dipole antenna. In this case, the ac voltage is a summation of optically induced antenna currents. For a half-wavelength dipole antenna, the voltage and electric field distributions are shown in Figure 3.

The antenna is divided into two quarter-wavelength dipoles (gray rectangles) with a diode at the center (white trapezoid).

Incident radiation induces a voltage across the dipole antenna with maxima at the ends of the antenna and a minimum at the center [8]. Therefore, the electric field and current distributions are a maximum at the center. To induce the maximum bias voltage across the diode, and thus generate the maximum tunneling current, the diode should be placed at the location where the voltage gradient is largest. This occurs where the electric field is a maximum at the center of the half-wavelength dipole antenna.
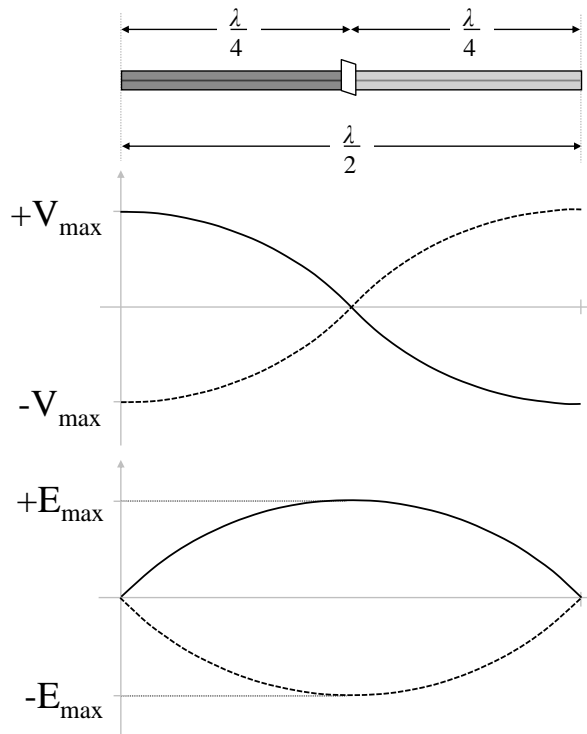
Figure 3: Current/Voltage distribution on a half-wavelength dipole antenna.

1.2 Circuit Model

The antenna-coupled MOM diode can also be represented with a circuit model. The diode is represented as a nonlinear resistance R_D in parallel with a junction capacitance and placed in series with an ac voltage source of real impedance R_A, as show in Figure 4 [9]. The series diode resistance is assumed to be negligible compared to the R_A and R_D.

From the circuit model, the effective voltage across the diode is

$$V_D = \frac{V_0 R_D}{R_A + R_D + j\omega C R_A R_D}, \tag{2}$$

where the junction capacitance $C = \varepsilon A/d$ is dependent on the contact area, oxide thickness, and oxide permittivity of the MOM structure. From Eq. (2), the power dissipated in the diode is

$$P_D = \frac{|V_D|^2}{2R_D} = \frac{V_0^2 R_D}{2[(R_A + R_D)^2 + \omega^2 C^2 R_A^2 R_D^2]} \tag{3}$$
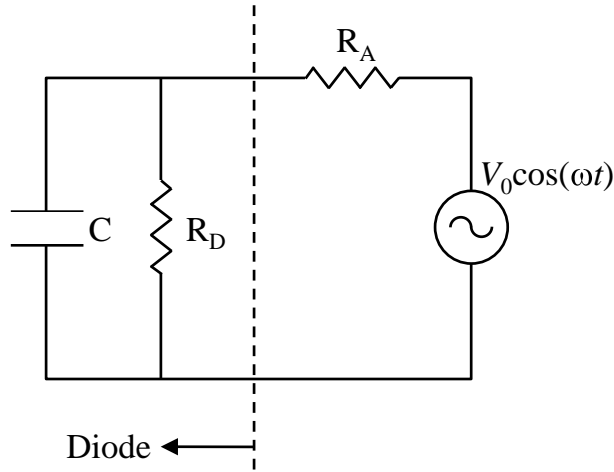
Figure 4: Equivalent circuit model for an antenna-coupled MOM diode.

For a fixed diode resistance R_D, optimal power transfer to the diode is obtained when the antenna resistance is minimized. This is contrary to the common impedance matching result where the antenna is matched to the load, the difference being that the load is held fixed while

the antenna resistance is varied [10]. This further motivates the use of a dipole antenna since the impedance at the feed point of a half-wavelength dipole is around 75 Ω.

Since the diode resistance is large compared the antenna resistance, the circuit can be approximated as series RC circuit with a cut-off frequency given by

$$f_c = \frac{1}{2\pi R_A C} = \frac{d}{2\pi R_A \varepsilon_0 \varepsilon_r A} \tag{4}$$

To achieve rectification at IR frequencies, the capacitance must be quite low. This is achieved most readily by reducing the junction area. With $R_A = 75\ \Omega$, $\varepsilon_r = 1$, and $d = 1$ nm, the overlap area required to achieve a cut-off frequency of 28.3 THz is approximately 90 nm $\times$ 90 nm.

1.3 Rectification Mechanism

In general, the dc or rectified component of the current is given by the time average of the current as [11]

$$I_{rec} = \frac{1}{2\pi} \int_{-\pi}^{\pi} I[V(t)] d(\omega t) \tag{5}$$

where $I[V(t)]$ is the current-voltage characteristic as a function of the time-dependent optical voltage. One can expand $I[V(t)]$ in a Taylor series with respect to voltage as

$$I[V(t)] = I(V_b) + \frac{dI}{dV}\bigg|_{V=V_b} V(t) + \frac{d^2 I}{dV^2}\bigg|_{V=V_b} V^2(t) + \dots \tag{6}$$

Evaluating the rectified current,

$$I_{rec} = \frac{1}{2\pi} \int_{-\pi}^{\pi} \left[I(V_b) + \frac{dI}{dV}\bigg|_{V=V_b} V(t) + \frac{1}{2} \frac{d^2 I}{dV^2}\bigg|_{V=V_b} V^2(t) + \dots \right] d(\omega t) \tag{7}$$

8

$$= \frac{1}{2\pi} I(V_b) \int_{-\pi}^{\pi} d(\omega t) + \frac{1}{2\pi} \frac{dI}{dV}\bigg|_{V=V_b} \int_{-\pi}^{\pi} V_0 \cos(\omega t) d(\omega t) + \frac{1}{4\pi} \frac{d^2 I}{dV^2}\bigg|_{V=V_b} V_0^2 \int_{-\pi}^{\pi} \cos^2(\omega t) d(\omega t) + \dots$$

This simplifies to

$$I_{rec} = I(V_b) + \frac{1}{4} \frac{d^2 I}{dV^2}\bigg|_{V=V_b} V_0^2 + \dots \tag{8}$$

For an unbiased diode, $I(V_b) = 0$ and the first nonvanishing term in the time average is

$$I_{rec} \approx \frac{1}{4} \frac{d^2 I}{dV^2}\bigg|_{V=V_b} V_0^2. \tag{9}$$

The proportionality constant is the nonlinearity of the diode. Its value is given by the second derivative of the *I-V* characteristic evaluated at the bias voltage. Thus, the rectified current is proportional to the square of the amplitude of the optical voltage, and therefore, to the infrared power at the MOM junction [7]. Eq. (9) is a semi-classical expression that relates the rectified current, a quantum mechanical quantity, to the classical optical power. As such, Eq. (9) allows one to calculate a quantity proportional to the rectified current using a classical electromagnetic solver.

The value of the nonlinearity can be calculated from the Schrödinger equation for a trapezoidal barrier with heights ϕ_i and thickness *d*. To first order, the wavefunction in the oxide is represented as an exponential expanded in a Taylor series. The total tunneling current is obtained by integrating over the contribution of electrons with different energies. To first order, the rectified current at zero bias is given by [12]

$$I_{rec} \approx \frac{1}{4} \frac{d^2 I}{dV^2}\bigg|_{V=V_b} V_0^2 \approx \frac{m_e^{1/2} d}{12 \hbar R_D} \frac{\phi_1 - \phi_2}{(\phi_1 + \phi_2)^{3/2}} V_0^2, \tag{10}$$

where m_e is the electron mass and $\hbar$ is Planck's constant. Inserting the expression for the sheet resistance, the rectified current can be written as

$$I_{rec} \approx \frac{m_e^{1/2}A}{6\hbar\rho}\frac{\phi_1-\phi_2}{(\phi_1+\phi_2)^{3/2}}V_0^2 \tag{11}$$

where ρ is the resistivity of the oxide layer, which in general is frequency dependent. Therefore, the primary design parameters are the barrier heights, overlap area, and resistivity of the oxide layer. The overlap area is bounded from below by fabrication limitations and above by the requirement that the capacitance enable rectification at IR frequencies. Since the barrier heights are the difference between the metal work functions and the conduction band of the oxide, the rectified current is proportional to the work function difference between the two metals. Therefore, we choose Aluminum (Φ_{Al} = 4.28 eV) and Platinum (Φ_{Pt} = 5.65 eV) to form an asymmetric MOM diode [13].

1.4 Fabrication, Characterization, and Modeling

Antenna-coupled MOM diodes are fabricated using electron beam lithography, electron beam evaporation, and vacuum chamber oxidation [13, 14]. By performing the metal depositions at opposing angles, the two metals overlap beneath a suspended bridge of undercut electron beam resist. Aluminum and platinum are chosen for their work function contrast and high conductivity in the IR [15]. The thickness of each metal layer is 30 nm. Prior to the Pt layer deposition, oxygen is released into the vacuum chamber at 100 mTorr, allowing the Al to grow a 10-15 Å thick native oxide. The lead lines, bond pads, antenna-coupled CPS, and diode are

10

deposited without breaking vacuum in the evaporation chamber. For a complete discussion of the fabrication process, see Appendix A.

Figure 5 contains a scanning electron micrograph of a completed antenna-coupled MOM diode. A superset SEM taken at high magnification shows a MOM diode that is circular in shape and approximately 100 nm in diameter. The dc component of the rectified current is transmitted to the bond pads through the electrical leads. Figure 6 shows the *I-V* characteristic for a typical Al/AlO$_x$/Pt MOM diode, including the current, resistance, and nonlinearity as a function of voltage. Deviations from these *I-V* characteristics can be expected. For example, the dc resistance varies from 1-10^3 kΩ and zero-bias nonlinearity varies from 1-10^2 μA$\cdot$V^{-2} [15].
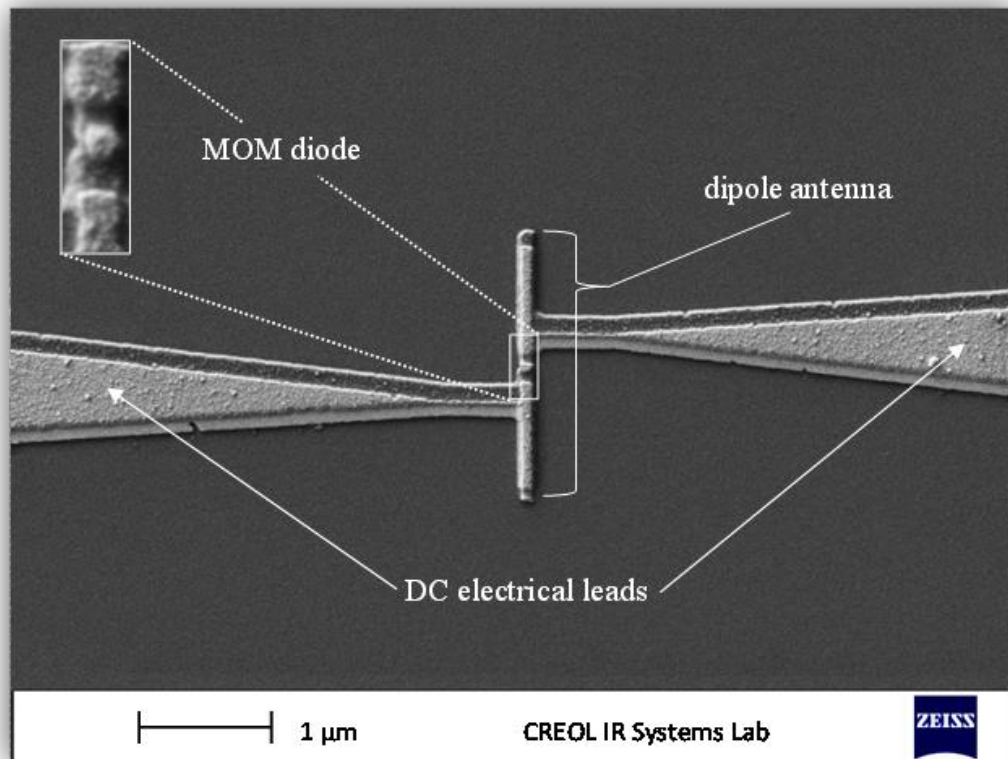
Figure 5: Scanning electron micrograph of a dipole antenna-coupled MOM diode infrared detector. The dipole is 100 nm wide and 60 nm thick. Inset: detail of the MOM diode overlap area, which is approximately 75 x 75 nm.
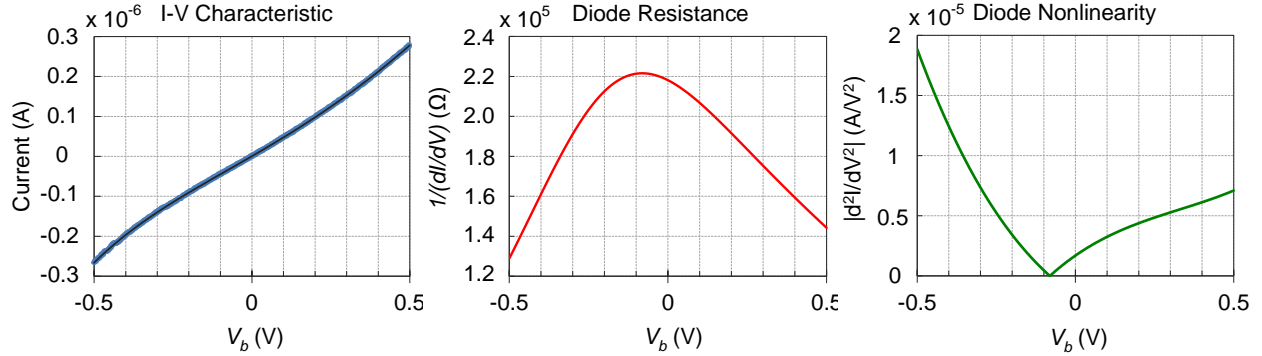
Figure 6: Current, resistance, and nonlinearity as a function of voltage for a typical Al/AlO$_x$/Pt MOM diodes.

At zero bias, the diode resistance is around 220 kΩ with a nonlinearity of 0.2 A·V^{-2}. This non-zero value of nonlinearity at zero bias enables sensor functionality without applied bias. A recent study details the effects of oxidation pressure on the dc resistance and nonlinearity of MOM diodes [15]. In general, the diode resistance increases with oxidation pressure while the zero-bias nonlinearity decreases with increasing resistance.

Numerical simulations are performed in Ansys High Frequency Structure Simulator (HFSS), a commercial electromagnetic finite element solver. In HFSS, the antenna structure is modeled in detail, including the overlapping metals from the shadow evaporation as well as the intermediate aluminum-oxide layer. Material properties, including refractive index and film thickness, are measured using a J.A. Woollam Infrared Variable-Angle Spectroscopic Ellipsometer (IR-VASE) and incorporated into the electromagnetic models to increase the accuracy of the simulations [16]. For a complete discussion of the electromagnetic simulations, see Appendix B.

12

1.5 Infrared Measurement Setup

The experimental IR setup is shown in Figure 7. Measurements are conducted with a 10.6 μm CO_2 laser. A beam splitter is used to redirect a fraction of the energy to a power meter for calibration. Several neutral density filters are used to control the amount of optical power falling on the device. A quarter-wave plate is used to rotate the linearly polarized radiation exiting the laser. The laser is mechanically chopped at 1.5 kHz at the focus of a ZnSe lens. By chopping the laser at 1.5 kHz, ambient 60 Hz noise and some thermal sources can be avoided. The laser is then passed through a collimating ZnSe lens and focused at F/8 onto the phased-array antenna, which is connected to a five-axis goniometer [17]. The rectified current from the diode is passed through an external current preamplifier and monitored with a lock-in amplifier that is referenced to the frequency of the mechanical chopper. Temporal fluctuations in the laser power are removed by dividing the rectified current by the reference power. All measurements are conducted without applied bias and with a laser irradiance of approximately 10 W·cm^{-2}, well within the region where the MOM diode acts as square law detector [15]. For all devices, the response to radiation polarized perpendicular to the dipoles is nearly equal to the Johnson noise, which indicates that the thermal and dc lead line contributions are negligible.
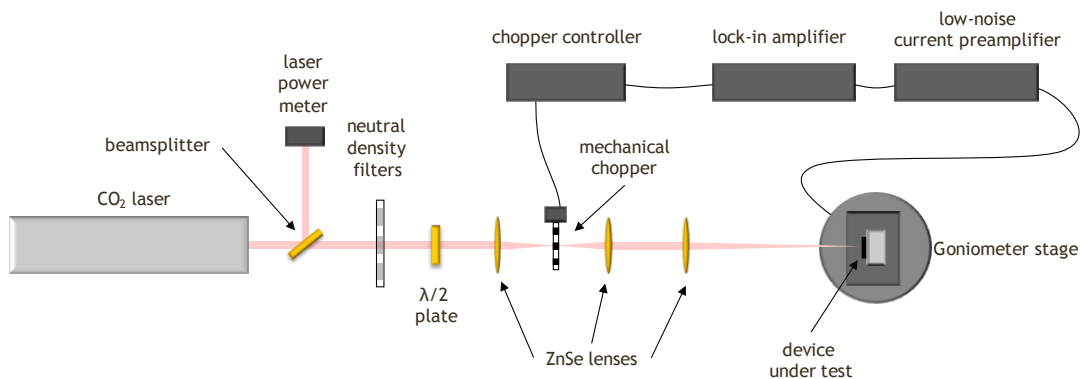
Figure 7: Experimental configuration for IR measurements.

One of the most common antenna characteristics is the angular response pattern. By measuring the angular response pattern, one can determine in what direction the antenna responds most efficiently. Through the Lorenz theorem of reciprocity [8], the angular response pattern can also referred to as a radiation pattern because the antenna responds in exactly the same fashion as it would potentially radiate. Typically, the angular response pattern is measured in either the E-plane or the H-plane. Both are shown in Figure 8. During an H-plane radiation pattern measurement, the polarization of the radiation is oriented along the dipole antenna while the goniometer is rotated in the plane perpendicular to the axis of the dipoles. Alternatively, for an E-plane radiation pattern measurement, the polarization of the radiation is still along the dipole antenna, as it must be, but the goniometer is rotated along the dipole antenna. In this thesis, we focus on the H-plane angular response pattern for reasons pertaining to the radiation characteristics of phased-arrays.
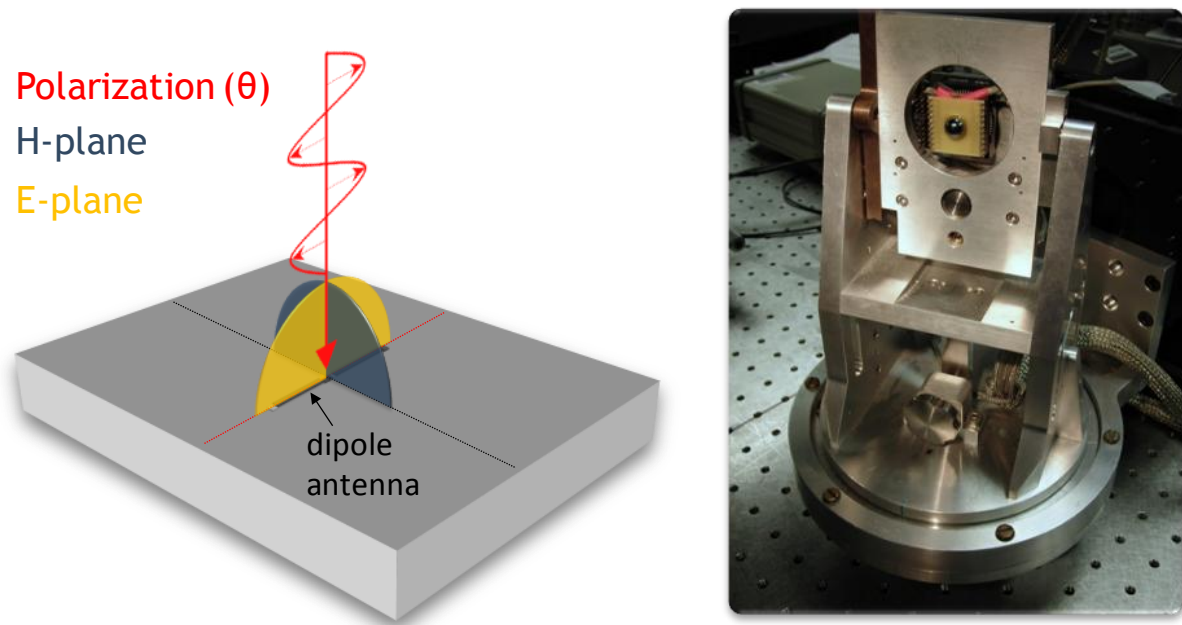
Figure 8: Definition of E- and H-planes for radiation pattern measurements.

To demonstrate the validity of the simulation technique, consider the antenna response as a function of the polarization angle of the incident radiation. Experimentally, the polarization of the incident radiation is altered by varying the angle of the half-wave plate. Ideally, the cross-polarized response will be zero, but in reality there is Johnson noise associated with the resistance of the diode. To account for this in the simulation, we include a constant offset in the simulated response. Figure 9 shows the measured antenna response along with the HFSS simulation. Excellent agreement is observed as the polarization is rotated through 2π radians.
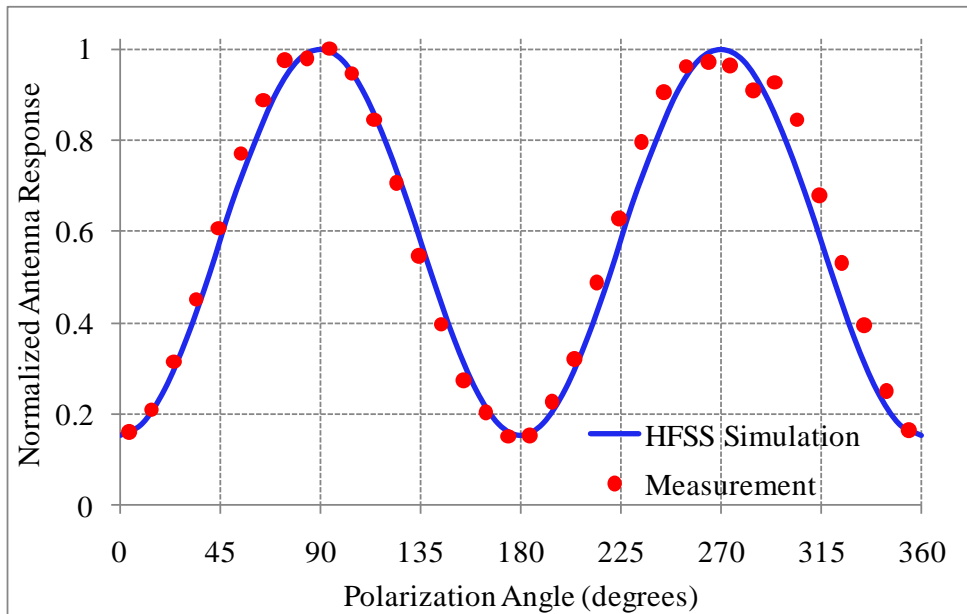
Figure 9: Polarization response of antenna-coupled MOM diodes.

1.6 Summary

Infrared detectors can be divided into three main categories: quantum or photodetectors, thermal detectors, and radiation field detectors. Photodetectors rely on the quantum nature of the electromagnetic field and its interaction with the quantized energy levels of semiconductor materials. Thermal detectors operate on the basis of voltage variations with optical power caused

by the variation of detector resistance with temperature. Although both detection mechanisms are appropriate for certain applications, radiation field detectors have the advantage that the coupling element, i.e. the antenna, can be tailored to achieve the desired polarization and wavelength response. A common antenna-coupled detector is the microbolometer, a thermal detector with a sensitivity determined by the TCR. Although microbolometers are readily integrated into antenna arrays, microbolometers exhibit distributed impedance due to poor TCR contrast between the antenna and bolometer [2]. To circumvent this issue, the microbolometer can be replaced with a MOM diode. MOM diodes operate on the basis of electron tunneling through an insulator layer electron upon excitation from radiation. The tunneling of electrons leads to a nonlinear *I-V* characteristic and thus to rectification of high frequency antenna currents at zero bias. Since the tunneling current is localized at the MOM overlap, the tunnel diode can be regarded as an infrared point detector.

MOM diodes are fabricated with electron-beam lithography, electron beam evaporation, and vacuum chamber oxidation. By performing the metal depositions at opposing angles, the two metals overlap between a suspended bridge of undercut electron beam resist. Aluminum and platinum are chosen for their large work function contrast and high conductivity in the IR. The thickness of each metal layer is 30 nm. Prior to the Pt layer deposition, oxygen is released into the chamber to allow the Al layer to grow a native oxide. The lead lines, bond pads, antenna, and diode are deposited without breaking vacuum in the evaporation chamber.

The dc component of the rectified current is proportional to the square of the optical voltage, or the optical power, impinging on the oxide. Therefore, a connection is established

between a quantum mechanical quantity, the rectified current, and the classical optical power allows one to simulate the relative response of the MOM diode to infrared radiation.

Infrared measurements are conducted with a 10.6 μm CO_2 laser. The rectified current from the diode is passed through an external current preamplifier and monitored with a lock-in amplifier that is referenced to the frequency of the mechanical chopper. Temporal fluctuations in the laser power are removed by dividing the rectified current by the reference power. During an H-plane radiation pattern measurement, the polarization of the CO_2 laser is oriented along the dipole antennas while the goniometer is rotated in the plane perpendicular to the axis of the dipoles.

To verify the accuracy of the simulation approach, we measure the antenna response as a function of the polarization angle of the incident radiation. In order to obtain agreement between simulation and measurement, a constant offset term must be included to account for several noise sources, including Johnson from the MOM diode dc resistance and contributions from the dc lead-lines.

17

CHAPTER 2: SUBSTRATE-SIDE ILLUMINATION USING IMMERSION LENS

Infrared antenna-coupled detectors are typically fabricated on planar substrates and illumination is provided from the air side. However, as mentioned in passing in Chapter 2, substrate-side illumination through a hemispherical immersion lens has the potential for additional signal to noise ratio gains [18, 19]. This can be understood qualitatively as follows. A dipole antenna responds to the parallel component of the local electric field. In the case of air-side illumination, the transmitted electric field in the dielectric is low compared to the incident electric field because the permittivity is higher. For substrate-side illumination, the transmitted electric field is greater than the incident field and the antenna response is increased. This can be explored experimentally by fabricating a dipole antenna on the flat surface of a hemispherical lens. For plane-wave illumination, the incident field is normal to the curved surface and no refraction will occur. In this context, the hemispherical lens can be regarded as an immersion lens, or dielectric half space.

2.1 Antenna on Air-Dielectric Interface

Consider Figure 10, in which an ideal dipole with current I_1 produces a field E_1 at the location of the test dipole I_2 [20]. Similarly, I_2 produces a field E_2 at the location of I_1. We regard I_2 as a test dipole that can be located in either region 1 or region 2. The field E_i is the electric field of an ideal current element in air. In the case where the currents are equal, $I_1 = I_2$, the Lorentz theorem of reciprocity requires that $E_2 = E_1$. Therefore, if we can calculate the value of E_2 at the location of I_1, then we can determine the value of E_1 at the test location I_2.
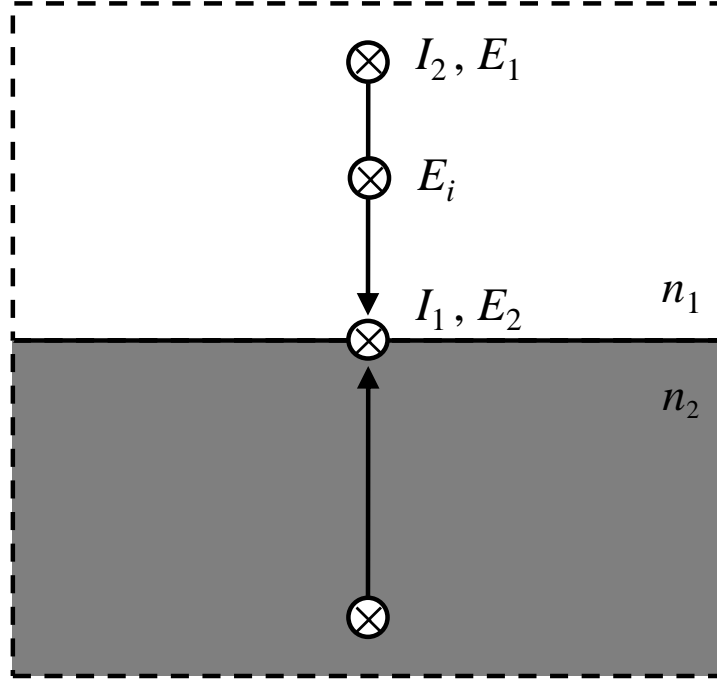
Figure 10: Definition of terms for calculating power radiated by a dipole antenna at an air-dielectric interface.

First consider the test dipole located in region 1. The field E_2 is proportional to the incident field multiplied by the TE transmission coefficient t_{12} from region 1 to region 2. Therefore, by reciprocity, the electric field E_1 is

$$E_1 = t_{12}E_i. \tag{12}$$

For normally incident illumination, the transmission coefficient is

$$t_{12} = \frac{2n_1}{n_1 + n_2}. \tag{13}$$

Therefore, the time averaged power density in region 1 is

$$S_1 = \frac{1}{2}n_1|t_{12}E_i|^2 = \frac{1}{2}n_1|E_i|^2\left(\frac{2n_1}{n_1 + n_2}\right)^2. \tag{14}$$

If the test dipole is in region 2, the field E_2 is proportional to the incident field multiplied by the transmission coefficient from region 2 to region 1. In this case, the time-averaged power density in region 2 is

$$S_2 = \frac{1}{2} n_2 |t_{21} E_i|^2 = \frac{1}{2} n_2 |E_i|^2 \left(\frac{2n_2}{n_2 + n_1} \right)^2 . \tag{15}$$

Adhering to our definition for the gain, we take the ratio of the power radiated into region 2 to the power radiated into region 1 to obtain

$$\Gamma \equiv \frac{S_2}{S_1} = \frac{n_2}{n_1} \left(\frac{2n_2}{n_2 + n_1} \right)^2 \left(\frac{n_1 + n_2}{2n_1} \right)^2 = \frac{n_2}{n_1} \left(\frac{n_2}{n_1} \right)^2 = \left(\frac{\varepsilon_2}{\varepsilon_1} \right)^{3/2} , \tag{16}$$

where we have used the fact that $\varepsilon_i = n_i^2$. In the case where region 2 represents the hemispherical immersion lens and region 1 is air, the gain can be written as

$$\text{Gain} \equiv \frac{\text{substrate-side response}}{\text{air-side response}} = \left(\frac{\varepsilon_{r,subs}}{\varepsilon_{r,air}} \right)^{3/2} \tag{17}$$

where $\varepsilon_{r,subs}$ and $\varepsilon_{r,air}$ are the relative permittivities of air and the lens [20, 21]. In this treatment, the immersion lens is assumed to be perfectly AR coated and the irradiance of the incident radiation is assumed constant. When the hemispherical surface of the immersion lens is not AR coated, Γ decreases dramatically. For example, a germanium immersion lens with a permittivity of $\varepsilon_{r,Ge} = 16$ at 10 µm generates a broadside responsivity gain of $\varepsilon_{r,Ge}^{3/2} = 64$ for a perfectly AR coated lens versus a gain of $\varepsilon_{r,Ge}^{1/2} = 4$ for an uncoated lens [18]. If the signal gain is to be maintained over the angular response pattern of the device, the AR coating must be uniform over the hemispherical surface. Otherwise, interference fringes would be apparent in the angular response due to the variations in path length for different angles of incidence. To satisfy the

20

condition for impedance matching at the germanium-air interface, the material we use for the AR coating must have a refractive index $n = \sqrt{n_{Ge}n_{air}} = 2$. One possible option is zinc sulfide (ZnS), a low-loss insulator (k = 0.017) with a refractive index of $n = 2.21$ at 10.6 μm. Since our measurements are performed around a narrow band at 10.6 μm, a single quarter wave layer of zinc sulfide will suffice with a thickness of 1.2 μm.

2.2 AR-Coating Deposition Techniques

AR-coated spherical lenses are used in telecommunication systems as low-cost fiber-to-fiber couplers [22]. In another application, AR-coated hemispherical microlenses are fabricated onto the end of an optical fiber to provide efficient coupling to a semiconductor laser [23]. For most intents and purposes, the deposition method of choice is low-pressure chemical vapor deposition (LPCVD) [24, 25] in which the non-planar substrate is placed in a vacuum chamber and heated to near 500° C. Several precursor gases are bled into the chamber at a pressure of 0.1-5 Torr. As the temperature increases, the precursor gases react and subsequently decompose isotropically onto all exposed surfaces of the substrate, resulting in a nearly perfect conformal coating.

In cases where the CVD recipe is unknown or when the toxicity of the precursors requires an elaborate or expensive experimental set-up, electron-beam or thermal evaporation may be the preferred method. For instance, the CVD process for ZnS usually involves separate sources of zinc and sulfur, which have a tendency to react prematurely, producing highly toxic gases such as $Zn(C_2H_5)_2$ and H_2S [26]. Moreover, the high temperatures required by the LPCVD process might be incompatible with materials having a low melting point (e.g., aluminum).

21

Physical vapor deposition is inherently directional because the vapor originates from a point source. As a result, it generally produces non-uniform films when evaporated on non-planar substrates. In our approach, the hemispherical lens is tilted relative to the source, and rotated throughout the deposition. We experimentally found that a rotation angle of 70º generates a relatively uniform film with less than 10 % thickness variation over the hemispherical surface. In addition, a theoretical model is developed and compared to contact surface profilometry measurements.

In order to test the impact of the AR coating on the signal gain, we fabricate a single dipole antenna onto the flat surface of a germanium immersion lens and measure the device response for both air-side and substrate-side illumination. Measurements at 10.6 μm indicate that excitation from the substrate-side yields an antenna response 49 ± 2.7 times greater than air-side illumination.

2.3 AR Coating on Hemispherical Lens

Figure 11 shows a photograph of the apparatus used to rotate the lens during the deposition. The thermal source at the bottom of the photograph is aligned with the center of curvature of the hemispherical lens. A white arrow is included to indicate the direction of rotation of the shaft. An analytical expression for the film thickness distribution over the lens surface can be derived from a radiometric analysis. To this end, consider a lens of radius R with its center of curvature coincident with the origin of the coordinate system shown in Figure 11(a).

22

Figure 11: Rotating device inside the evaporation chamber. The hemispherical lens is 14 cm above the thermal source and rotated in a direction indicated by the white arrow.
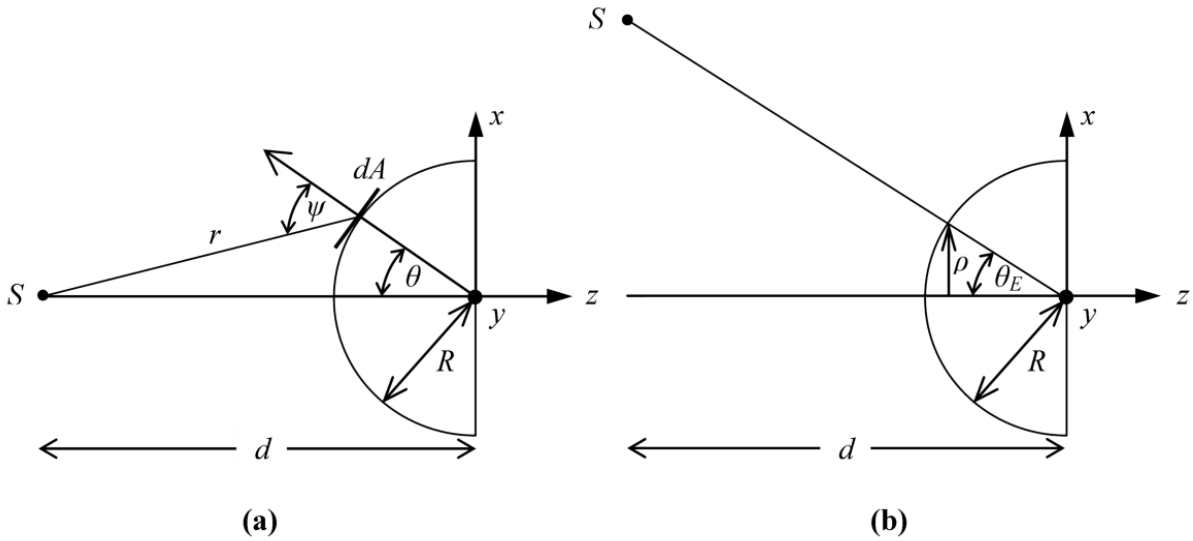
Figure 12: Geometric definition of terms for the radiometric analysis with a point source on-axis (a) and oriented at an angle θ_E relative to the center of curvature of the lens (b).

The evaporation source S, which can be either electron-beam or thermal, is regarded as a point source located on the z-axis a distance d from the center of curvature of the lens. The number of particles per unit time ϕ originating at the source, falling on the infinitesimal surface element dA is given by the product of the intensity I, in particles per steradian per unit time, and the solid angle as

$$\phi = I\Omega = I\frac{dA\cos\psi}{r^2}, \tag{18}$$

where ψ is the angle between the radius vector r and a vector normal to dA. The irradiance E, in particles per unit area per unit time, is given by

$$E = \frac{\phi}{dA} = I\frac{\cos\psi}{r^2} = I\left[\frac{d^2\cos^2\theta - 2dR\cos\theta + R^2}{(d^2 - 2dR\cos\theta + R^2)^3}\right]^{1/2}. \tag{19}$$

Here the cosine and sine laws were used to eliminate the variables r and ψ and obtain the irradiance in terms of measured quantities.

If the distance from the source to the center of curvature is much greater than the radius of the lens ($d \gg R$), Eq. (19) simplifies to

$$E \approx E_0\cos\theta, \tag{20}$$

where $E_0 = I/d^2$ is a constant proportional to the film thickness. Eq. (20) corresponds to the case in Figure 12(a), where the source is aligned with the pole of the hemispherical surface.

In the limit where $d \gg R$, the film thickness distribution can be projected onto the $z = -R$ plane at the front surface of the lens. The coordinates in this plane are related to the angle θ by

$$\sin\theta = \frac{1}{R}\sqrt{x^2 + y^2}. \tag{21}$$

24

Inserting this expression into Eq. (20) and simplifying yields

$$E(x, y) = E_0 \cos\left[\sin^{-1}\left(\frac{1}{R}\sqrt{x^2 + y^2}\right)\right] = E_0 \sqrt{1 - \frac{x^2 + y^2}{R^2}} . \tag{22}$$

A change in the evaporation angle shifts the center of the cosine distribution in Eqs. (20) and (22), as shown in Figure 12(b), while the effect of the lens rotation is to average $E(x, y)$ over one angular period. Therefore, the thickness distribution of the rotated hemispherical lens is given by

$$E(x, y; \rho) = \frac{E_0}{2\pi} \int_0^{2\pi} \sqrt{1 - \frac{(x - \rho\cos\theta)^2 + (y - \rho\sin\theta)^2}{R^2}} d\theta . \tag{23}$$

Here, the notation $E(x, y; \rho)$ denotes the film thickness as a function of the x and y coordinates, evaluated at the spatial offset ρ, which is the x-direction distance from the z-axis to the new center of the cosine distribution, as shown in Figure 12(b). The spatial offset is related to the evaporation angle θ_E by the expression

$$\sin\theta_E = \frac{\rho}{R} , \tag{24}$$

where θ_E is defined in Figure 12(b) as the angle between the source and z-axis, measured from the center of curvature. The thickness distribution can be rewritten in terms of the evaporation angle as

$$E(x, y; \theta_E) = \frac{E_0}{2\pi} \int_0^{2\pi} \sqrt{1 - \frac{(x - R\sin\theta_E \cos\theta)^2 + (y - R\sin\theta_E \sin\theta)^2}{R^2}} d\theta . \tag{25}$$

The integral in Eq. (25) cannot be solved analytically. As a check, Eq. (25) simplifies to the static, non-rotating case of Eq. (22) when the evaporation angle is zero.

Figure 13 shows the film thickness distribution in Eq. (25) for evaporation angles of 0°
and 70°. Since the source distance and intensity remain constant, the theoretical curves are
normalized so that $E_0 = I/d^2 = 1$. When the hemispherical lens is directly above the source
(θ_E=0°), the film thickness follows a cosine distribution, as shown in Figure 13(a). As the
evaporation angle increases, more material is deposited at the edge of the lens, resulting in
increased film uniformity.
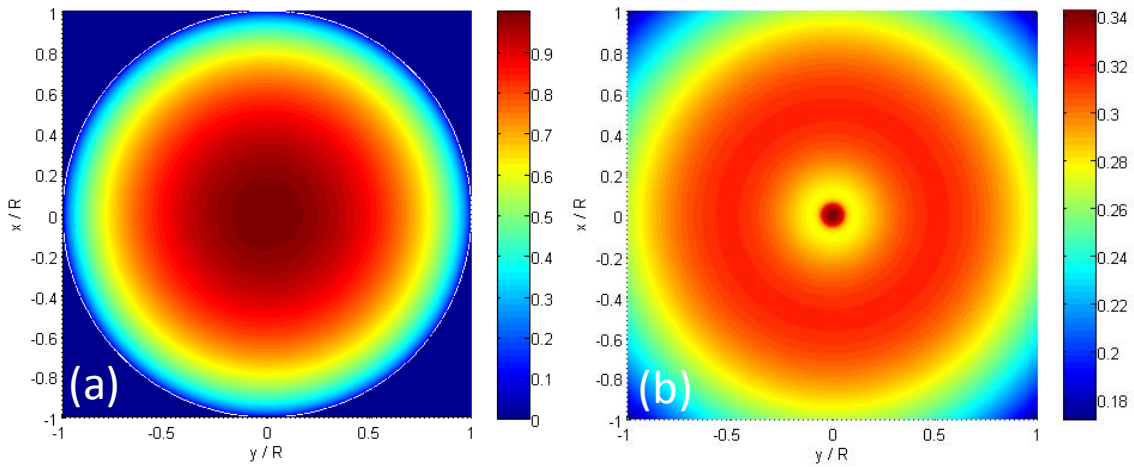
Figure 13: Normalized film thickness (E/E_0) from Eq. (25) for source angles of 0° (a) and 70° (b).

As shown in Figure 11, the hemispherical lens is located well above the thermal boat
(d=14 cm, R=0.5 cm). A crystal thickness monitor is located on the left side of the chamber. The
rotating device consists of an electric ac gear motor and a Variac control, which is connected to
the gear motor via an electrical vacuum feed-through. Prior to installation, the motor was out-
gassed in a test chamber at ~1 mTorr for 36 hours. A custom aluminum holder secures the
hemispherical lens to the rotating shaft. For all depositions, the rotation rate was set to 0.1 rev·s^{-1}
on the external Variac control. The model and results are not dependent on the rotation rate as
long as the duration of the deposition is much greater than one period of rotation.

Assuming that adhesion and mechanical stress issues are negligible, the model and results are independent of the lens material and evaporant. The hemispherical lens is a high-resistivity 3.3 Ω cm germanium lens with a permittivity $\varepsilon_r = 16$, a 10 ± 0.01 mm diameter, a thickness of 5 ± 0.05 mm, and a surface quality of 60/40 scratch/dig. In all depositions, the evaporant is zinc sulfide, a low-loss insulator with a refractive index of $n = 2.21$ in the 10 μm infrared region. A BOC Edwards Auto 306 evaporation system, compatible with both electron-beam and thermal sources, is used to thermally evaporate zinc sulfide at a rate of ~1.2 nm·s^{-1}. Five film thickness measurements were taken in 15º increments from zero to 60º using a Veeco Dektak 3 Surface Profiler and variable angle stage. The profilometer scan range was a 300 μm region at the top surface of the lens.

Figure 14 contains a cross-sectional plot of Eq. (25) at $y = 0$ for three different evaporation angles. The thickness is plotted as a function of the incident angle θ, defined in Figure 12(a). Since the source distance and intensity remain constant, the theoretical curves can be normalized so that $E_0 = I / d^2 = 1$. In practice, two evaporations are required at each angle: one to determine the thickness for an arbitrary tooling factor, and another with the adjusted tooling factor. The data points are normalized to the theoretical curves using a least squares fit, and the error bars represent one standard deviation above and below the mean.

In agreement with Eq. (20), a cosine distribution is obtained when the evaporation angle is zero. As the evaporation angle is increased to 45º, the thickness at broadside (zero degrees) decreases relative to the thickness at large angles. For an evaporation angle of 70º, the measured thickness variation is less than 10 % over a 120º full angle of the hemispherical surface. For larger evaporation angles, the broadside thickness tends to zero. The abrupt decrease in thickness

that is expected around 17º for an evaporation angle of 45° is not present in the measurements. This feature is an artifact of the model, which assumes that areas not directly exposed to the source receive zero flux. In reality, a moderate amount of residual vapor is expected, and will diminish this feature substantially. To account for this, a constant thickness offset must be added to Eq. (25). This is further justified by the fact that zinc sulfide has a relatively high vapor pressure of $\sim 10^{-5}$ Torr, and may outgas during chamber evacuation.

The thickness offset can be determined from the impingement flux of an ideal gas [27]. By calculating the total number of ZnS molecules impinging on the hemispherical surface over the duration of a deposition, the thickness of a shell of molecules on the lens surface can be determined. During a typical ZnS deposition, the temperature and pressure within the chamber are around 50 ºC and 10^{-5} torr, respectively. Under the assumption that the residual vapor behaves as an ideal gas under these conditions, the thickness of a homogeneous shell of ZnS molecules formed on the hemispherical surface during a 15 minute deposition is 350 nm, or approximately 30 % of the total AR coat thickness of 1.2 μm. Therefore, a thickness offset of $0.3E_0$ is added to Eq. (25) prior to normalization. This has the effect of flattening the distribution over the lens surface.
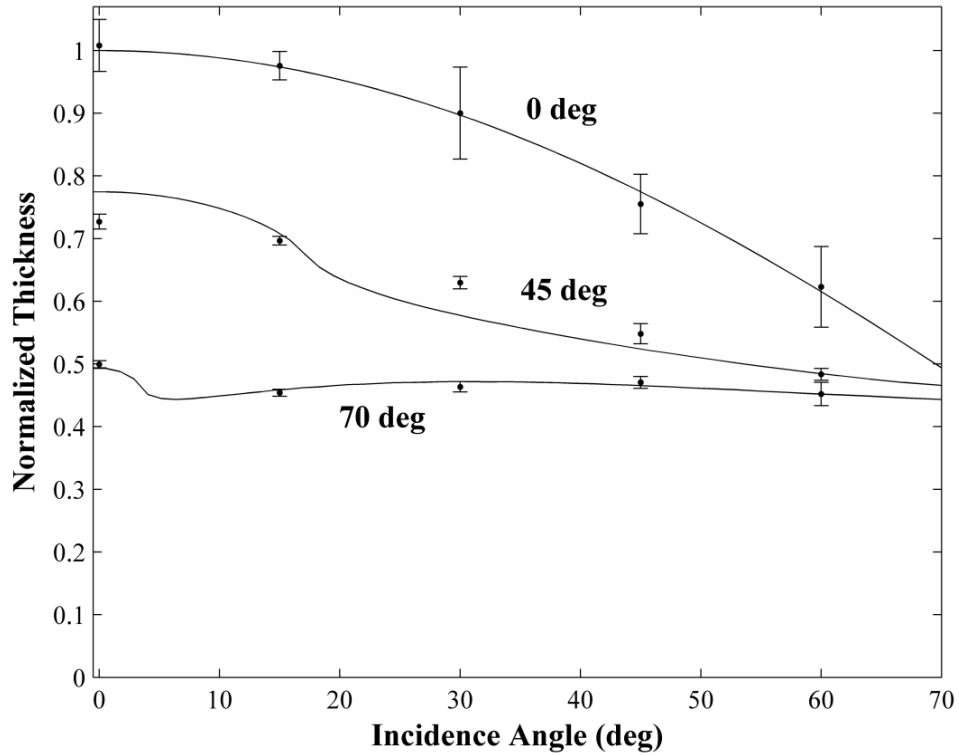
Figure 14: Film thickness as a function of the incident angle for evaporation angles of 0°, 45°, and 70°. Measurements are normalized to the theoretical curves by minimizing the mean squared error, and error bars represent one standard deviation above and below the mean.

2.4 Substrate-Side Gain Measurements

To test the impact of the AR coat on the irradiance responsivity ratio, a single dipole and bolometer were fabricated onto the flat surface of a hemispherical lens (Figure 15) using a Leica EBPG5000+ electron beam writer [28]. A resist bilayer was used, consisting of polymethyl methacrylate-methyl acrylic acid 9 % and 150 nm of 950 K polymethyl methacrylate. Both layers were baked on a hot plate at 180 ℃ for 10 min. Following the exposure, the resist was developed for 60 seconds in a 1:3 mixture of methyl isobutyl ketone:isopropanol. The fabrication process consisted of two electron beam writes: one for the antenna, lead lines, and alignment marks, and another to align the bolometer with the feed point of the dipole. For both exposures,

the dose and beam current were 620 $\mu C/cm^2$ and 25 nA, respectively. The gold antenna and nickel bolometer were deposited using electron-beam evaporation in the BOC Edwards system.

The antenna was illuminated with a CO_2 laser operating at 10.6 μm. The laser was modulated at 2.5 kHz using a mechanical chopper and a bias voltage of 100 mV DC was applied across the antenna [18]. The output signal from the device was measured using a lock-in amplifier and a computer with LABVIEW.
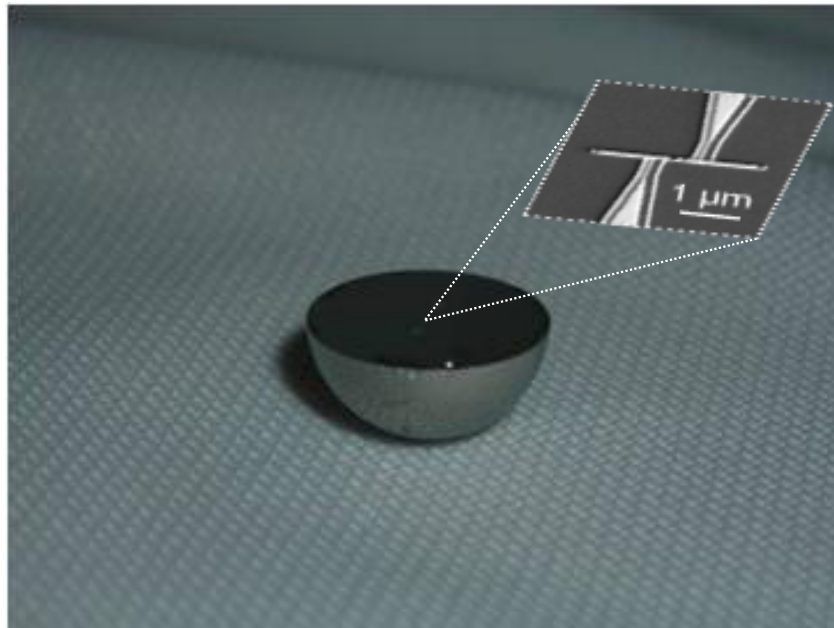
Figure 15: Fabrication of antenna onto the flat surface of a hemispherical immersion lens.

Unfortunately, the reflectance at the curved surface cannot be measured directly, since reflections from the flat surface are also present. However, a gain measurement can provide information regarding the performance of the AR coating. The theoretical broadside gain is plotted in Figure 16 for both an uncoated and AR coated lens [18]. The measurements represent the average and standard deviation for three different single dipole devices.

For the uncoated germanium lens with permittivity $\varepsilon_{r,Ge} = 16$, the measured gain was 3.6 ± 0.2, in good agreement with the theoretical value of 4. The measured gain for the AR coated lens was 49 ± 2.7, a significant increase, but less than the expected value of 64. Errors can be attributed to the film thickness and misalignment. Further refinement of the AR coat thickness will likely close the gap between the theoretical and measured gain.
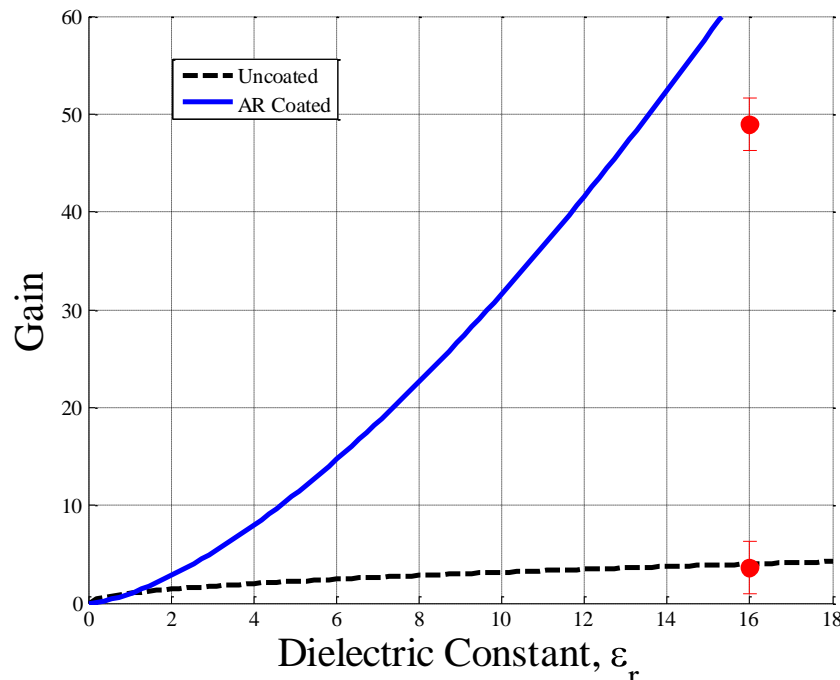
Figure 16: Gain as a function of the dielectric constant of an uncoated and AR coated immersion lens. The measurements represent the average and standard deviation for three different dipole devices fabricated onto the flat surface of a germanium immersion lens. The AR coating is a single-layer of zinc sulfide with a quarter-wave thickness of 1.2 μm.

2.5 Summary

An antenna on the flat surface of an immersion lens receives radiation more efficiently when illuminated through the substrate. The antenna response increases dramatically when the permittivity of the immersion lens is large and the curved surface is AR coated. For the large signal gain to be maintained for all illumination angles, the AR coat must be uniform over the

curved surface. As an alternative to LPCVD, a simple evaporation for depositing a uniform film on the hemispherical lens was presented. In this process, the curved surface is tilted relative to the source, which can be either electron-beam or thermal, and rotated throughout the deposition. Rotation at an angle of 70º generates a film with less than 10 % thickness variation over a 120º full angle of the immersion lens. A theoretical model was developed and compared to profilometer measurements. In all cases, general agreement between measurement and theory has been demonstrated. A single dipole was fabricated onto the flat surface of an AR coated germanium immersion lens. Substrate-side illumination generates an antenna response 49 ± 2.7 times greater than air-side illumination.

CHAPTER 3: ALTERNATE SUBSTRATE CONFIGURATIONS

The angular-response characteristics of an antenna are determined by boundary conditions imposed by the surrounding dielectric or conductive environment on the radiated fields of the antenna [29]. In the simplest case, the antenna sits on the interface of a dielectric half space and illumination originates from the air or the substrate side. In the laboratory, a single interface can be replicated by a hemispherical immersion lens [18]. If the device is fabricated onto the flat surface of the hemisphere, the incident propagation vector will remain normal to the curved surface and no refraction occurs. In this configuration, significant gains in responsivity are observed when a high-index lens is properly AR coated [30].

The resistivity of Al/AlO$_x$/Pt diodes is much greater than common semiconductor materials. When the MOM diode is fabricated directly onto a semiconductor substrate, the dc component of the rectified current will bypass the diode and flow into the semiconductor substrate. To avoid a conduction path in the substrate, the MOM diodes must be fabricated onto a thin electrical insulating layer. To study the influence of the substrate on the angular response pattern of infrared dipole antennas, three unique configurations are considered: a planar substrate with an insulator layer above a ground plane, germanium hemispherical lens substrate with insulator layer, and the latter with an additional insulation layer and ground plane [31].

3.1 Hemispherical Lens with Insulating Film

Consider a hemispherical lens with a thin insulating film, as shown in Figure 17. A TE polarized plane wave is incident at an angle θ on a dipole antenna with its long axis pointed into

the page. A thin electrical insulator layer of refractive index n_f and thickness d electrically isolates the antenna from the conductive substrate. Since the MOM diode acts as a square-law detector, the measured response is proportional to the optical power incident on the diode. Therefore, the measured response will be proportional to the total time averaged power density at the air-film interface.
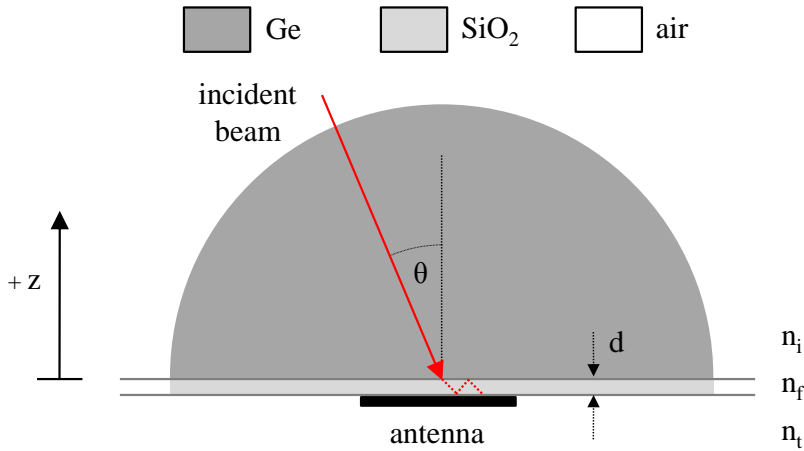
Figure 17: Cross sectional illustration of a device fabricated on a thin insulator film on a hemispherical immersion lens. The incident beam is normal to the curved surface and therefore aligned with the device at the center of the flat surface of the lens.

For plane-wave illumination, the time-averaged power density is proportional to the squared norm of the transmission coefficient for the interface. For a thin film, the TE transmission coefficient can be written as [32]

$$t = \frac{(1+r_{tf})(1-r_{if})e^{-i\delta}}{1-r_{tf}r_{if}e^{-i2\delta}} \qquad (26)$$

where r_{tf} is the reflection coefficient at the bottom interface in Figure 17, r_{if} is the reflection coefficient at the top interface, and δ is the phase shift due to propagation in the film layer

$$\delta = \frac{2\pi}{\lambda_0}d\sqrt{n_f^2 - n_i^2 \sin^2\theta} \qquad (27)$$

where λ_0 is the wavelength of incident radiation in free space, d is the thickness of the film, n is the refractive index of the respective materials, and θ is the angle of incidence. The thickness d is taken to be negative since the angle of incidence is measured relative to the film-air interface, not the substrate-film interface. The reflection coefficients r_{12} in Eq. (26) are given by

$$r_{12} = \frac{n_1 \cos\theta - \sqrt{n_2^2 - n_1^2 \sin^2\theta}}{n_1 \cos\theta + \sqrt{n_2^2 - n_1^2 \sin^2\theta}} \tag{28}$$

Figure 18 shows the H-plane angular response pattern of a single half-wavelength dipole fabricated on a 47 nm layer of SiO_2 illuminated through the Germanium hemispherical lens.
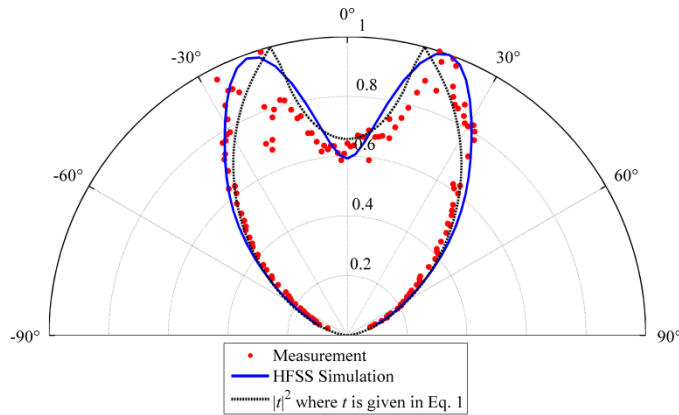
Figure 18: H-plane angular response pattern of a dipole antenna fabricated on 47 nm film of SiO2 on a germanium hemispherical lens. The peak in the angular response corresponds to the critical angle between germanium and air.

Not surprisingly, the angular response pattern closely resembles that of an antenna fabricated directly onto a hemispherical lens [18]. There is good agreeement between the simulated (blue line), analytic (gray line), and measurements (red points). The peaks in the angular response pattern correspond to the critical angle between air and germanium. Variations from the expected response are attributed to film thickness variations from a quarter-wavelength AR coat. Deviations from the a perfect AR coating tend to enhance reflections from the curved

surface of the germanium lens. The full-width half-maximum (FWHM) beam width is approximately 90°.

Figure 19 shows the H-plane angular response pattern for a dipole antenna identical to the one in Figure 18 fabricated on a 169 nm layer of SiO_2 . As before, the device is illuminated through the hemispherical substrate. There is close agreement between the measured data, the HFSS simulation, as well as the squared nrom of the transmission coefficient. As before, the peaks in the H-plane angular response occur at the cricitcal angle between the germanium and air. The pattern is narrowed from the 47 nm layer case, with a FWHM of approximately 75°.
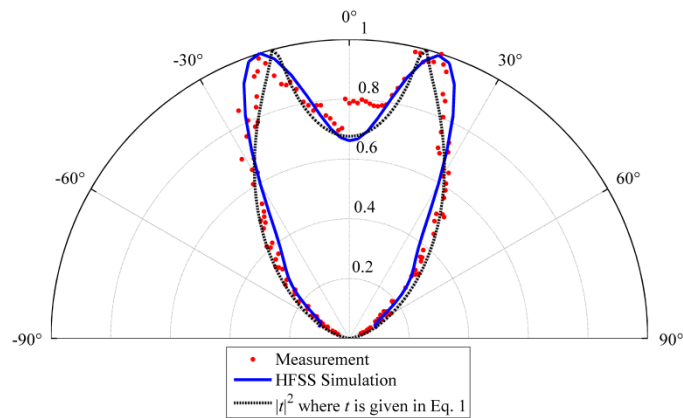
Figure 19: H-plane angular response pattern of a dipole antenna fabricated on 169 nm film of SiO_2 on a germanium hemispherical lens.

Figure 20 shows the H-plane angular response of the same antenna on a 475 nm layer of SiO_2. Close agreement is observed between the measured data, HFSS simulation, and squared norm of the transmission coefficient. The angular response pattern is narrowed from the 169 nm SiO_2 layer case to approximately 50° FWHM. Increasing the SiO_2 thickness beyond 475 nm does not further narrow the pattern, but instead lowers the broadside response. The broadside response would continue to decrease as the film thickness approaches one quarter wavelength.
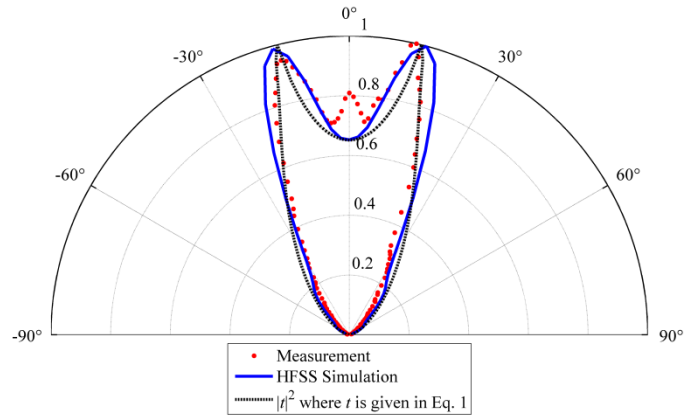
Figure 20: H-plane angular response pattern of a dipole antenna fabricated on 47 nm film of SiO_2 on a germanium hemispherical lens.

The narrowing of the radiation pattern can be explained in terms of the interference between the incident field and the wave reflected from the substrate-film interface. As the film thickness increases, the propagation phase shift between the incident and reflected radiation increases. Consequently, the degree of destructive interference also increases. Since the propagation length of the reflected beam increases for large angles, a decrease in transmitted power is observed at large angles, resulting in a narrowed angular response pattern.

3.2 Dielectric Layer Above Ground Plane

Consider the substrate configuration in Figure 21. The dipole antenna is fabricated on a thin dielectric layer above a 100 nm aluminum ground plane. A Si wafer is used for mechanical support. In this configuration, the antenna responds to incident radiation as well as radiation reflected from the ground plane. From reciprocity, one could attempt to calculate the far field radiation pattern of the antenna by considering the intereference between the antenna and its image behind the ground plane. However, we choose to model the antenna in receiving mode to be consistent with the measaments.

37

In this case, the transmission coefficient is the product of the transmission coefficient for the air-dielectric interface and an additional interference factor to account for reflections from the ground plane,

$$t_{GP} = t\,[1 + \exp(i\varphi)] \qquad (29)$$

where φ is the phase shift due to round-trip propagation in the dielectric layer,

$$\varphi = \frac{4\pi h}{\lambda_0}\sqrt{n_t^{\,2} - n_i^{\,2}\sin^2\theta} \pm \pi. \qquad (30)$$

Here, h is the thickness of the dielectric, which in this case is BCB, and the π phase accounts for the reflection from the ground plane. To simplify the expressions, the ground plane factor only accounts for the first reflected wave. From Eq. (28), the intensity of the second reflected wave from the BCB-air interface at broadside is only 4 %.
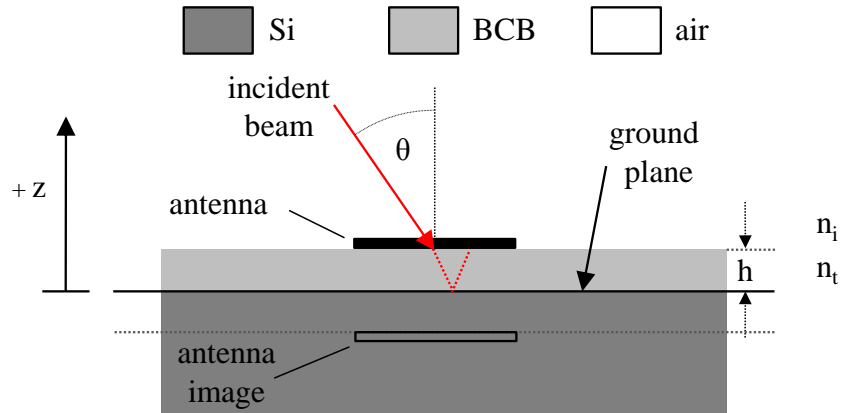
Figure 21: Cross-sectional view of a dipole antenna fabricated on a planar substrate with a 1.8 μm layer of BCB above a ground plane. Radiation is incident from the air side. The device responds to incident radiation as well as radiation reflected from the ground plane.

Here, h is the thickness of the dielectric, which in this case is BCB, and the π phase accounts for the reflection from the ground plane. The ground plane factor only accounts for the first reflected wave in order to simplify the expressions.

The measured angular response of a 3.4 μm half-wavelength dipole in the H-plane with the ground plane configuration above is shown in Figure 22. The data points represent the measured data, the solid blue line represents the HFSS simulation, and the dotted black line indicates the squared norm of the transmission coefficient in Eq. (29), where $n_s = 1$ for air-side illumination, $d = 0$ μm, and $n_a = 1.55$ for BCB, and includes the ground-plane factor, where $h = 1.6$ μm and $n = 1.55$ for BCB.
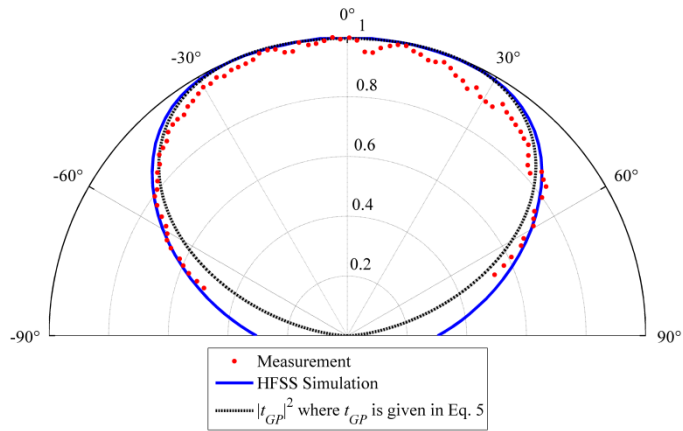
Figure 22: H-plane angular response pattern for dipole antenna fabricated on a 1.8 μm BCB dielectric layer above a ground plane.

The measured data is in excellent agreement with both the HFSS simulations as well as the analytic expression derived from the transmission coefficient with the ground plane image factor. Compared to the previous two configurations, this substrate yields the broadest angular response pattern in the H-plane, with a FWHM of approximately 140°. We find later that a broad angular response pattern enables beam steering as it represents the angular range that is accessible to a phased-array.

3.3 Hemispherical Lens with Insulating Film, Dielectric Layer, and Ground Plane

The final substrate configuration is a combination of the previous two. The antenna is fabricated on a thin electrical insulation layer on the flat surface of a hemispherical lens, as shown in Figure 23, with an additional quarter-wavelength SiO_2 layer and ground plane. The H-plane angular-response pattern for this configuration is shown in Figure 24.
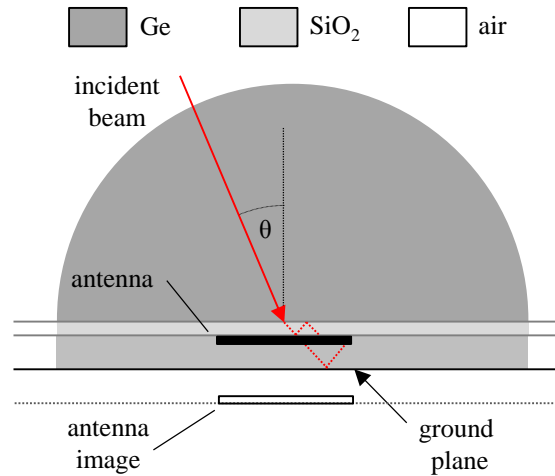
Figure 23: Cross-sectional illustration of a dipole antenna fabricated on a hemispherical substrate with a 475 nm layer of SiO_2, capped with a layer of SiO_2 and aluminum ground plane.

In this case, the analytic expression is the squared norm of the transmission coefficient in Eq. (29), where t is the transmission coefficient for a SiO_2 film separating the Ge and SiO_2 half-spaces. Again, there is good agreement between the HFSS simulation and analytic expression with the measured data. The FWHM is approximately 40-50°. Thickness nonuniformities on the bottom SiO_2 layer are likely responsible for the deviations from the expected response. There were apparent film adhesion issues between the two SiO_2 layers following the ground plane deposition.
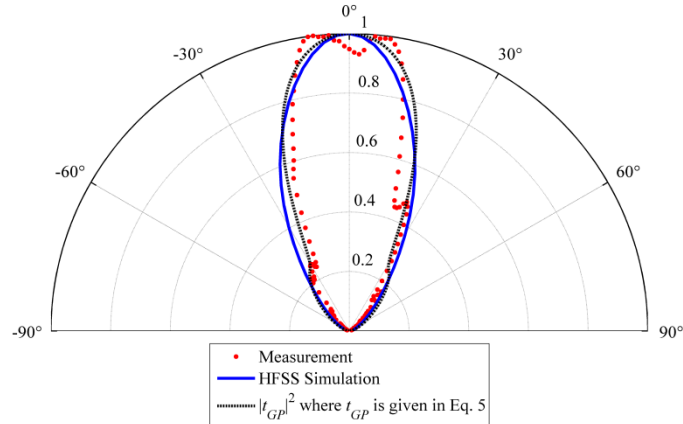
Figure 24: H-plane angular response pattern of a dipole antenna fabricated on a hemispherical substrate with a 475 nm layer of SiO_2, capped with a layer of SiO_2 and aluminum ground plane.

This series of measurements demonstrates the influence of the substrate configuration on the H-plane angular response pattern of dipole antennas. The far-field radiation pattern is determined by boundary conditions imposed on the radiated fields. More specifically, the angular response pattern of a square-law detector, i.e. a MOM diode, is proportional to the total power density in the vicinity of the detector. For substrate-side illumination through a hemispherical immersion lens with an optically thin SiO_2 standoff layer (50 nm), the angular response pattern resembles that of a dipole fabricated directly on germanium. In general, as the thickness of the insulator layer increases, the radiation pattern narrows, which can be explained by the interference between the incident field with reflections from the film-substrate interface. Since the optical path length increases for large angles of incidence, the degree of destructive interference is greater for large angles, resulting in a narrowed radiation pattern.

The angular response pattern of a dipole fabricated on a 2.0 μm dielectric layer above a ground plane is broadened compared to the case where no ground plane is present. This arises from the constructive interference between the incident wave and reflections from the ground plane. Since the path length increases with the angle of incidence, the degree of constructive

41

interference increases for large angles. As a result, the power received by the antenna is greater for large angles of incidence, resulting in a broadened radiation pattern.

The final substrate configuration consists of a SiO_2 dielectric layer on a germanium hemispherical lens with an additional quarter-wavelength matching layer and ground plane. In this case, the FWHM is very similar to the case without the ground plane. In addition, the measured SNR for this configuration is approximately two times greater than without a ground plane.

3.4 Summary

The angular response pattern of an IR antenna is determined by the boundary conditions imposed on the electromagnetic fields in the vicinity of the device. For example, the angular response pattern of a single dipole on an interface is determined by the transmission coefficient for that interface. To further investigate this formalism, we fabricated single dipole antennas on several unique substrates: a planar substrate with an insulator layer above a ground plane, germanium hemispherical lens substrate with insulator layer, and the latter with an additional insulation layer and ground plane [23]. The angular response of a dipole on an insulator above a ground plane was found to be uniform and broad. In the context of phased-array antennas, this will prove to be very useful. When the devices are fabricated on a thin insulator layer on an immersion lens, the width of the angular response pattern is determined by the thickness of the film layer. This can be understood in terms of the interference between the incident field and that reflected from the film surface. As the film thickness increases, the degree of destructive interference between these fields increases. Since the path length in the film layer increases at

large angles, destructive interference is more pronounced at large angles, leading to a narrower angular response pattern. The final substrate configuration was a combination of the previous two. The antenna was fabricated onto a thin film on the flat surface of a hemispherical immersion lens. An additional dielectric layer and ground plane were then deposited on top of the device. In this configuration, the angular response pattern is narrow compared to the case where no ground plane is present.

CHAPTER 4: TAILORING OFF-BROADSIDE ANGULAR RESPONSE

For a single dipole antenna, the angular response pattern is determined by the surrounding dielectric and conductive environment. We found that the angular response can be narrowed by illuminating the antenna through a thin film or broadened by fabricating the devices on a dielectric layer above a ground plane. Similar to the analysis of radio-frequency antennas, the angular response pattern of a phased-array antenna consisting of several antenna elements is proportional to the product of an array factor and the radiation pattern of a single element [8]. By this approach, large steering angles are made accessible to an array by maximizing the width of the single-element radiation pattern. Of the various substrate configurations studied in Chapter 2, a dielectric layer above a ground plane was found to exhibit the broadest radiation pattern, nearly twice as broad as the angular response of the same antenna fabricated on a hemispherical substrate. Therefore, one expects larger steering angles to be accessible with this configuration. In addition, the presence of a ground plane leads to enhanced field confinement within the substrate and thus to a resonance which is more sensitive to changes in antenna length [33].

The angular response characteristics of phased-array antenna-coupled microbolometers are documented in the literature [19, 34]. A common antenna design utilizes a dipole antenna pair to capture and transfer the incident radiation to the microbolometer along a coplanar strip (CPS) transmission line [10, 35]. The position of the microbolometer relative to the dipoles determines the phase shift between the infrared currents. Although microbolometers are readily integrated into antenna arrays [36], the thermal detection mechanism diminishes their ability to operate as a point load.

44

With these considerations, we revisit the possibility of controlling the angular response pattern of infrared phased-array antennas. We do so by implementing a MOM diode to ensure that the measured response originates from a coherent summation of infrared antenna currents at a localized point in the array, and not from the distributed thermal response of the antenna, interconnects, and lead-lines. The reception angle of the antenna is altered by shifting the diode position along the CPS that connects the antenna elements. Substantial improvements in beam width and steering angle are realized by fabricating the antenna arrays on a fixed dielectric stand-off layer above a ground plane. Radiation patterns measured with a 10.6 μm CO_2 laser are corroborated with electromagnetic numerical simulations as well as an analytic interference model.

4.1 Method

Consider two dipole antennas connected by a CPS of length *L*, on a dielectric layer above a ground plane, with a diode placed a distance *d* from their common center, as shown in Figure 25. One can derive an expression for the reception angle of the antenna from the array factor for a two dipole array. A plane wave polarized along the direction of the dipoles (shown in red) is incident on the antenna at an angle *θ* measured from the surface normal in a plane perpendicular to the dipoles (H-plane).

| BCB | Aluminum | Platinum | Aluminum oxide |
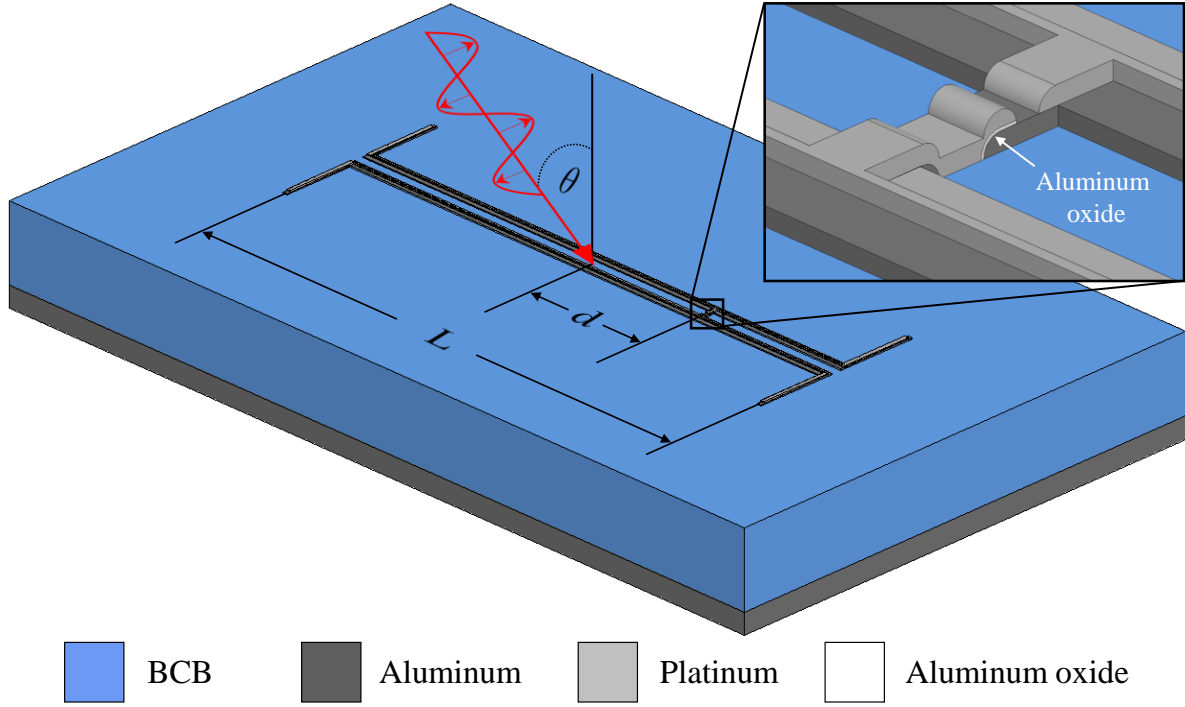
Figure 25: Model of the antenna/substrate configuration and definition of terms. Superset image shows the aluminum-platinum overlap and the aluminum oxide barrier. The angle θ is measured in the plane perpendicular to the dipoles (H-plane).

The radiation arriving at the detector will include a phase shift due to free space propagation that is angle dependent as well as an interelement phase shift acquired during propagation along the CPS. Constructive interference occurs at the diode when the total phase difference is an integer multiple of 2π,

$$\frac{2\pi}{\lambda_0} L \sin\theta_m - \frac{2\pi}{\lambda_0} 2n_m d = 2\pi m, \tag{31}$$

where λ_0 is the wavelength in free space and n_m is the effective index of the CPS mode. The response angle of the antenna array corresponds to the primary maximum in the interference pattern. Inserting $m = 0$ into Eq. (31),

$$\theta_0 = \sin^{-1}\left(\frac{2n_0 d}{L}\right). \tag{32}$$

As one might expect, the response angle of the antenna increases as the diode is shifted away from the center of the dipoles. For diode shifts that are small compared to the antenna spacing, the reception angle varies approximately linearly with the diode shift as $\theta_0 \cong 2n_0 d / L$. The magnitude of the response angle is determined by the ratio of the diode shift to the dipole separation. In the absence of dispersion, the response angle is independent of the illumination wavelength. A reduction in phase shift between antenna elements due to a change in wavelength is compensated for by a proportionate phase shift along the CPS transmission line.

4.2 Simulation and Design

Figure 26 contains scanning electron micrographs (SEMs) of two completed antenna-coupled MOM diode devices. The topmost, symmetric antenna is designed for broadside or normally incident illumination. In this case, the diode is centered between the dipole antennas. The bottommost antenna has the diode shifted $d = 3.3$ μm from center. This design is optimized for response at 50º. A high magnification SEM shows a MOM diode that is circular in shape and approximately 100 nm in diameter.

The coupling efficiency and attenuation constant of a CPS are determined by the strip separation and substrate material, respectively. To minimize absorption by the substrate, the CPS mode should lie symmetrically about the dielectric-air interface. Toward this end, we choose benzocyclobutene (BCB), a low loss insulator ($k = 0.015$) with a refractive index close to that of air ($n = 1.55$) in the 10.6 μm infrared region. To optimize the coupling efficiency from the antenna to the CPS, the diode response is monitored in HFSS while varying the strip separation. Including the overlap from the shadow evaporation (discussed below), a separation of 230 nm

yields the greatest antenna response. Similarly, one could attempt to optimize the coupling efficiency from the CPS to the MOM diode by changing the overlap area. The problem here is that the diode area is bounded from below by fabrication limitations and above by the requirement that the capacitance enable rectification at IR frequencies [4].
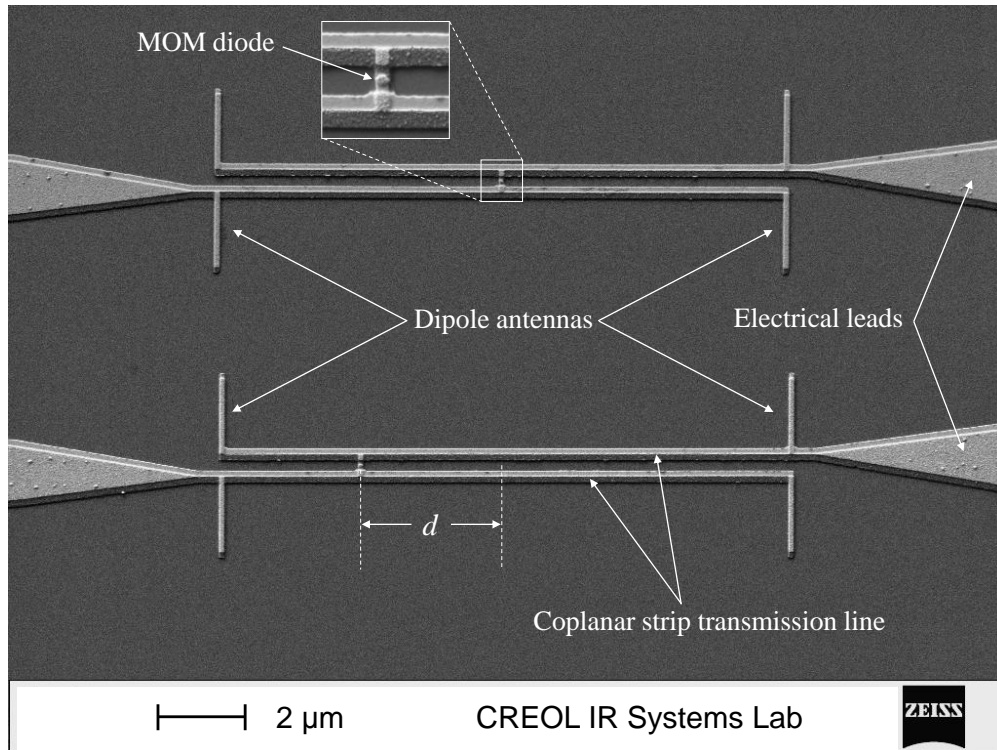
Figure 26: Scanning electron micrograph of the phased-array antenna with (top) a centered diode and (bottom) with the diode shifted by d = 3.3 μm. Superset SEM of the MOM diode shows an overlap that is circular in shape and approximately 100 nm in diameter.

The rectified current at the MOM junction is proportional to the optical power, or equivalently, the square of the electric field. For a half-wave dipole, the field will be a maximum at its center. Therefore, the rectified current will be maximized when the antennas are designed to resonate at one-half wavelength. For a BCB-air interface, the effective index is $n_{eff} \approx 1.3$, corresponding to an effective half-wavelength for the dipole of $\lambda_0 / 2n_{eff} \approx 4$ μm [13]. This value

is also identified in numerical simulations as the dipole length that generates the greatest response.

A parametric analysis is performed in HFSS to maximize the width and uniformity of the single element pattern. As the BCB thickness increases from zero, the radiation pattern broadens until it reaches a maximum width when the BCB thickness is one quarter wavelength. Beyond this, the radiation pattern develops a null at broadside. The optimal radiation pattern occurs for a thickness of 1.8 μm.

According to Eq. (32), the response angle of the antenna depends only on the ratio of the diode shift to the antenna spacing. However, one must also consider the near fields produced by the dipole antennas, and the effects they might have on the measured response [37]. To avoid any near-field interference, the antenna spacing should be sufficiently large so that the diode is removed from the reactive near field of the dipole antennas, which is generally taken to be around one quarter of the effective wavelength [8], or about 2 μm on BCB. By setting $d = 0$ and $m = 1$ in Eq. (31), one finds that the width of the main lobe in the radiation pattern varies as λ_0 / L so that larger antenna spacings produce narrower beam widths. However, as the antenna spacing increases, the infrared currents must travel a greater distance to reach the diode, and will thus be subjected to more attenuation. Moreover, the side-lobe contribution generally increases as the antenna spacing increases. Therefore, one chooses the maximum antenna spacing that simultaneously minimizes propagation loss and side lobe-level. Numerical simulations that include the measured material properties infer an optimal antenna spacing of $L = 12.9$ μm.

4.3 Measured Angular Response Patterns

The measured and simulated radiation patterns in the H-plane of a single dipole on a 1.8 μm BCB stand-off layer above a ground plane are shown in Figure 27. Both the measurement and simulation are normalized to their maximum values. The radiation patterns are plotted linear in power to emphasize the square-law behavior of the MOM diode. As expected, the single element radiation pattern is uniform and broad, with a FWHM of 140º. Since the overall radiation pattern is given by the product of the array factor and the single-element pattern, Figure 27 represents the range of reception angles that is accessible to an array. Excellent agreement is observed between the measured and simulated radiation patterns.
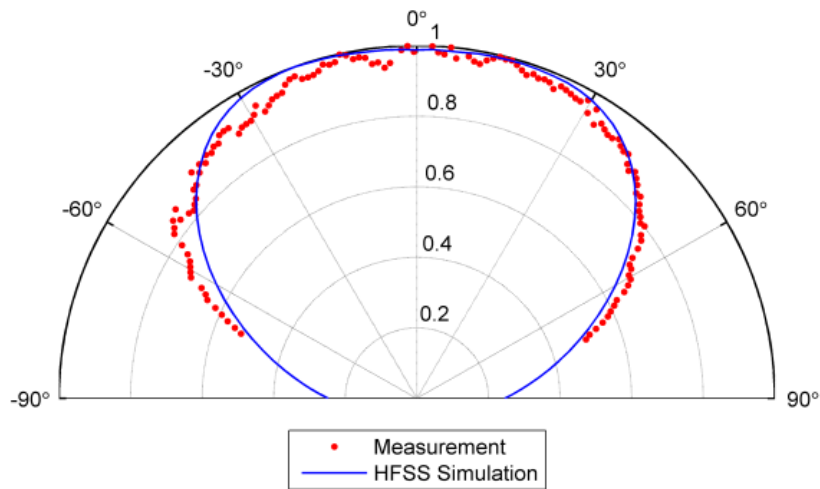
Figure 27: Measured and simulated radiation pattern (linear in power) of a single dipole on a 1.8 μm BCB stand-off layer above a ground plane.

Figure 28 shows the measured radiation patterns along with the HFSS simulations for antenna arrays with diode shifts of d = 0, 0.9, 1.8, and 3.3 μm. Over this range, the response angle of the antenna varies from 0º to 50º. Negative angles can be easily obtained by shifting the diode in the opposite direction. As the response angle increases, the FWHM increases slightly from 30º to 40º while the side lobe magnitude increases from 5 % to around 25 %. Excellent

agreement between simulation and measurement is observed for both the response angle and beam width.
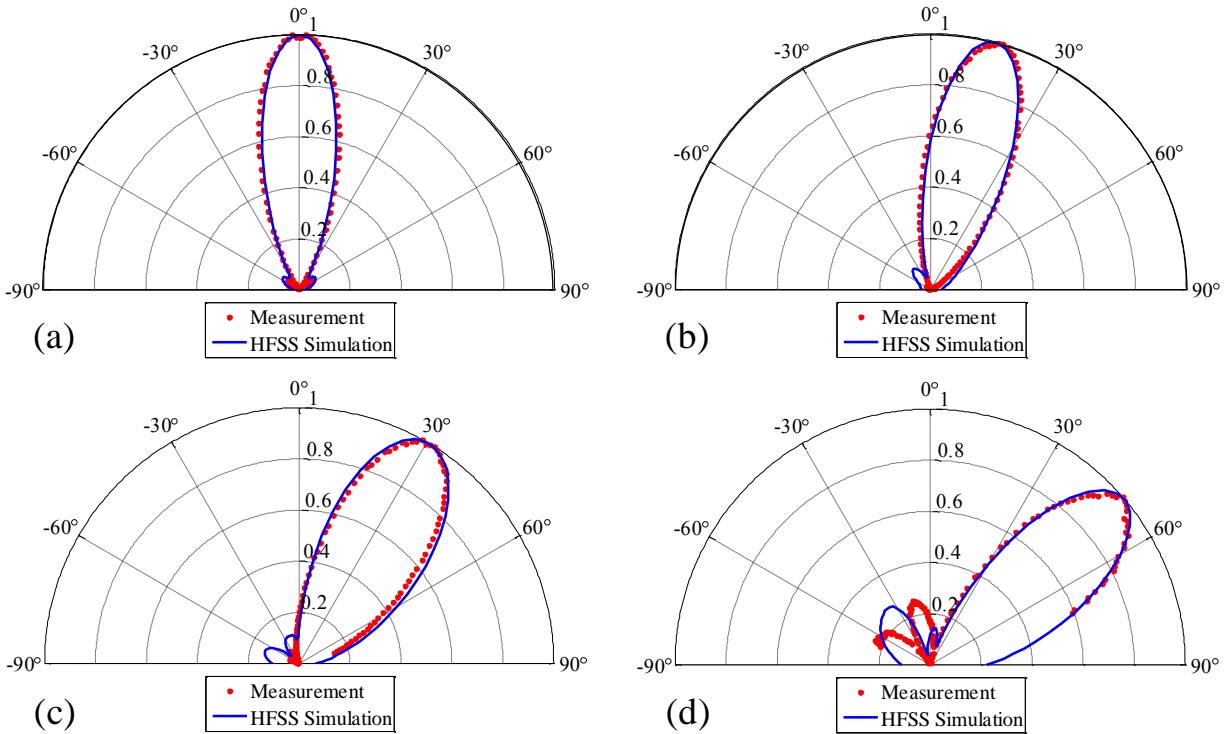
Figure 28: Measured and simulated radiation patterns (linear in power) of a dipole pair antenna on a 1.8 μm BCB stand-off layer above a ground plane with the diode shifted (a) d = 0 μm, (b) d = 0.9 μm, (c) d = 1.8 μm and (d) d = 3.3 μm.

Moderate discrepancies between simulation and measurement are apparent in side-lobe magnitude and angle, which may be attributed to alignment errors and uncertainty in the local substrate thickness. The alignment procedure ensures that the device is simultaneously aligned with the axis of rotation of the goniometer and focus of the laser beam to within approximately ± 12 μm. For a Gaussian beam of waist w_0 = 115 μm, a device displaced 24 μm in a direction perpendicular to the beam path would experience an 8 % reduction in power density, which partially accounts for the discrepancy in the side lobe level and position. In the simulations, the side lobe level and position are determined by the single-element pattern, which depends

primarily on the thickness of the dielectric layer. From ellipsometric measurements performed on the actual substrate containing the devices, the percentage deviation from the measured thickness is ± 1.6 %, significant enough to impact the side lobes in the simulations. Since the exact substrate thickness in the vicinity of each device is unknown, the best one can do is set the thickness in HFSS to the value measured with the infrared ellipsometer, which is essentially an average over an approximately 8 mm diameter beam.

4.4 Look-Angle Limits

A plot of the measured and simulated response angle as a function of the ratio of the diode shift to the antenna spacing is shown in Figure 29. The response angle is taken to be the angle where the radiation pattern is a maximum.
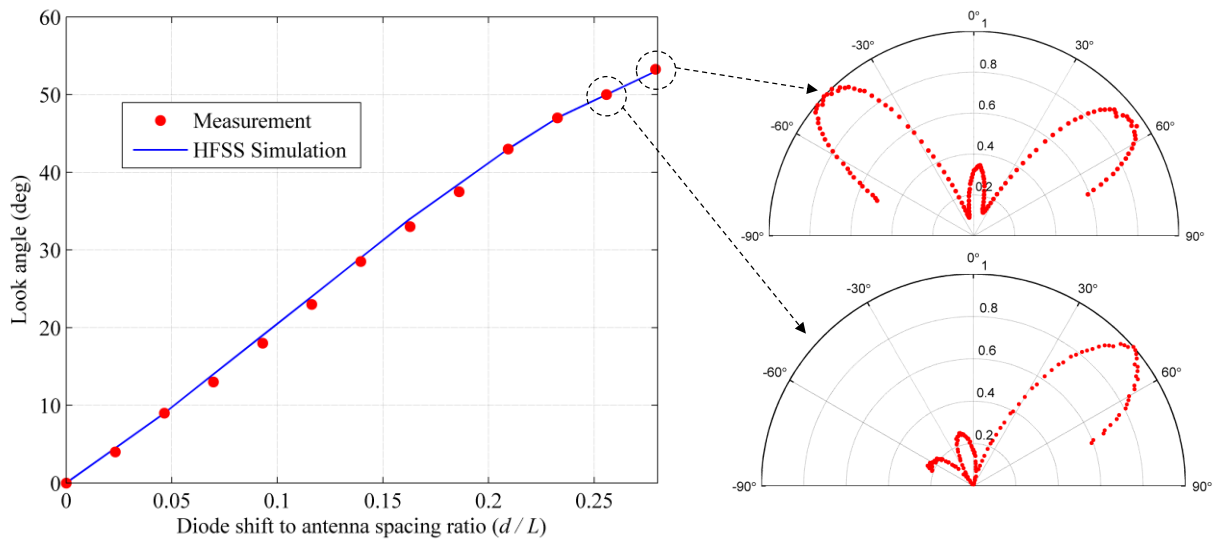
Figure 29: Measured and simulated response angle as a function of the diode shift to antenna spacing ratio d / L. All devices are fabricated on a fixed 1.8 μm BCB stand-off layer above a ground plane. Response angles beyond 50° are accompanied by an equal or greater side lobe response.

When the diode shift is small compared to the antenna spacing, the response angle varies linearly with the diode position, as prescribed by Eq. (32). For diode shifts greater than approximately one quarter of the antenna spacing, the response angle levels off, reaching a maximum around 53º. Since the total radiation pattern is given by the product of the array factor and the single-element pattern, the maximum response angle of the array corresponds to the angle where the single-element pattern decreases rapidly. From Figure 27, this occurs around 55º. Moreover, as the main lobe shifts towards large angles, the side lobes are magnified as they approach broadside. Consequently, response angles beyond 50º are accompanied by an equal or greater side lobe response, as shown in Figure 29.

4.5 Summary

For certain applications, it may be useful to alter the angular-response pattern of an antenna. With a single dipole, this can be achieved by altering the substrate on which the antenna is fabricated. In another approach, the substrate configuration is fixed while the antenna geometry is altered. One simple example is a two-element phased-array connected by a CPS transmission line. The spatial separation of the antennas leads to a phase difference between the antenna elements when the angle of incidence is off broadside. By shifting the diode relative to the antennas, one can compensate for this phase shift to achieve constructive interference between the antenna currents. Therefore, in this configuration the direction of maximum angular response is altered by shifting the diode position along the transmission line connecting the antenna elements.

In general, the angular response of the phased-array antenna is the product between the single element pattern and an array factor, which accounts for the interference between the antenna elements. Therefore, in order to achieve the maximum possible angular range of detection, the width of the angular response for a single element must be maximized. This can be achieved by fabricating the phased-arrays on a dielectric layer above a ground plane. With this substrate configuration, narrow beam widths of 35º FWHM in power and reception angles of ±50º are achieved with minimal side lobe contributions. For response angles beyond 50°, the main lobe in the radiation pattern is accompanied by an almost equal-amplitude side-lobe. Measured radiation patterns at 10.6 μm are substantiated by electromagnetic simulations as well as an analytic interference model.

CHAPTER 5: MULTIPLE-ELEMENT PHASED ARRAYS

A two-element phased-array antenna can be used to determine the angle of arrival of incident radiation. For a two-element phased array, one can compensate for a free-space phase shift introduced between the antenna elements for off-normal angles of incidence by shifting the location of the diode along the transmission line connecting the antenna elements. Although large angles of incidence are accessible with a two-element phased-array, the width of the angular response pattern, or angular resolution, is limited by the separation of the antenna elements, which is bounded from above by the emergence of grating lobes [38]. By increasing the number of elements while keeping the antenna separation fixed, the effective antenna aperture can be made larger, and the angular resolution narrower, without introducing grating lobes into the angular response [39]. Further improvement in angular resolution can be achieved by reducing propagation loss in the CPS transmission line [35, 40]. Toward this end, one can increase the confinement of electric fields between the coplanar strips by increasing the metal thickness. This has the effect of increasing the power density of the CPS mode by decreasing the cross-sectional area of the mode.

5.1 Method

Figure 30 contains electron micrographs of the phased arrays under consideration. The MOM diode is centered in the array and the dipole antennas are periodically spaced by a distance *d*. We have not included a dipole antenna at the location of the MOM diode. According to

simulation and measurement, the angular-response pattern in that case is almost completely determined by the center antenna since there is no propagation loss for that element.

Infrared radiation incident on the array induces electric fields with maxima at the center of the dipoles. A fraction of this energy is transferred to the CPS transmission line in the form of confined radiation and electrical currents. The electric field component that remains after propagation along the CPS generates a time-dependent bias across the MOM diode.
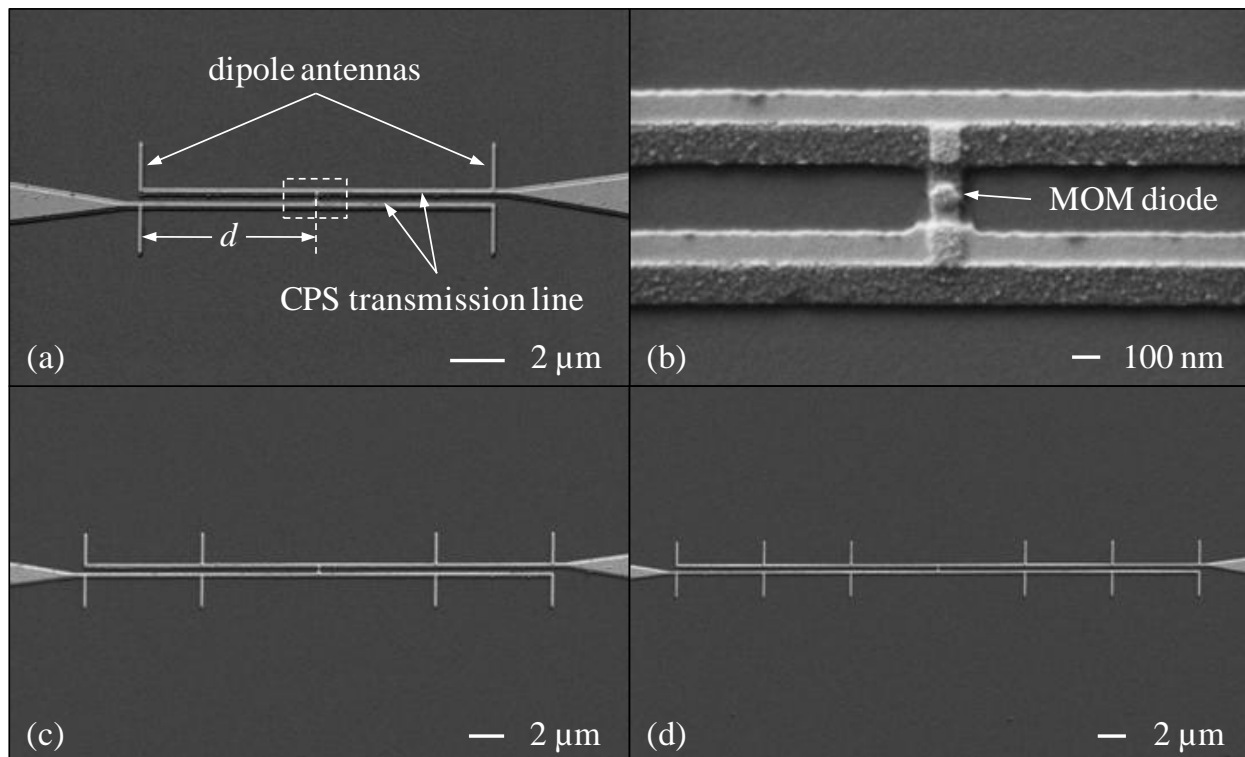
Figure 30: Electron micrographs of (a) two-, (c) four-, and (d) six-element infrared phased-array antennas.

An additional bias voltage is supplied by the short metallic strip that connects the CPS to the MOM diode (Figure 30 (b)). This contribution must be included because the axis of the strip is along the direction of the incident polarization. The metal strip can be modeled as a detuned dipole antenna with a real coupling efficiency $\kappa < 1$. The tapered dc lead lines do not contribute

significantly to the measured response because they are perpendicular to the incident polarization and large compared to the dipole antennas. This is confirmed by modeling and by measurement of a negligible cross-polarized response.

For a thin oxide layer, the optical voltage V_i supplied to the MOM diode is approximately proportional to the amplitude of the electric field at the junction. Its value depends on the electromagnetic boundary conditions imposed by the surrounding dielectric or conductive environment, which in general depend on the angle of incidence θ. If the diode is fabricated on a planar substrate, $V_i(\theta)$ is proportional to the magnitude of the electric-field amplitude transmission coefficient for the interface [20]. When the diode is integrated with a phased-array antenna, additional voltage sources are present with relative phase determined by the interference of CPS antenna currents at the location of the diode. Therefore, the array contribution depends on the angle of incidence, the element spacing d, number of antenna elements N, and the CPS attenuation constant α. With these considerations, the total bias voltage induced across the diode can be written as

$$V_0(\theta) = V_i(\theta)\left[\kappa + \sum_{m=1}^{N/2}\cos\left(m\frac{2\pi}{\lambda_0}d\sin\theta\right)\exp(-m\alpha d/2)\right], \qquad (33)$$

where λ_0 is the free-space wavelength and the summation accounts for the contribution of additional antenna elements. The applied voltage takes the conventional form of the product of the element pattern with an array factor [8].

From the discussion leading up to Eq. (33), one finds that the width of the angular response pattern can be narrowed in several ways. In the simplest case, no array is present (a single antenna) and the angular response pattern is determined by $V_i(\theta)$. In this case, one can

tailor the angular response of the device by manipulating the substrate configuration [31]. When the phased array is included, the magnitude of its contribution is determined by the number of antenna elements and the CPS propagation loss. The purpose of this chapter is to determine how these mechanisms influence the angular response pattern of infrared phased-array antennas.

When additional antenna elements are included in the array, the effective aperture of the antenna increases. Because of diffraction, a wider aperture produces a narrower angular response. This effect is apparent in Eq. (33) since the contribution to the voltage from the outer elements is a modulation with increased angular frequency. However, if the propagation loss is large, the IR currents generated by the outer elements are attenuated when they reach the diode. As a result, the modulation term in Eq. (33) is diminished and the angular response resembles the single-element pattern $V_i(\theta)$, which for typical substrate configurations is quite broad [31]. If the propagation loss is negligible, the modulation term is comparable in magnitude to κ, leading to a modulation that decreases rapidly with the angle of incidence and thus to a narrowed angular response pattern.

5.2 Simulation and Design

In HFSS, a quantity proportional to the rectified current is computed as the power dissipated in the aluminum-oxide volume. The power dissipated represents the amount of electromagnetic energy that is converted to thermal energy. To simulate the $F/8$ measurement setup (discussed below), the antenna is excited in HFSS with a Gaussian beam of waist $w_0 = 115$ μm with wavelength 10.6 μm (28.3 THz). A radiation pattern is generated by computing the power dissipated in the oxide volume for each angle of incidence [41].

Primary design considerations include the substrate configuration, antenna length and spacing, CPS separation, and metal thickness. From Eq. (33), the total voltage supplied to the MOM diode is given by the product of the single element pattern $V_i(\theta)$ with an array factor. In order to produce the widest single-element pattern, the devices are fabricated on a quarter-wavelength dielectric layer above a ground plane [31]. The dielectric is a 1.7 μm layer of benzocyclobutene (BCB), a low loss insulator ($k = 0.015$) with a refractive index of $n = 1.55$ in 10.6 μm infrared region. The use of a low-index substrate also reduces inhomogeneities in the dielectric environment, leading to increased symmetry in the near fields and reduced propagation loss in the CPS [35].

The antenna length and CPS separation are chosen to optimize power transfer from free-space radiation to guided modes in the CPS [41, 42]. This is accomplished in HFSS by terminating a CPS transmission line with a MOM diode and monitoring the response while varying the CPS separation and antenna length. From a parametric analysis in HFSS, the optimal antenna length and CPS separation are 4 μm and 470 nm center-to-center, respectively. This antenna length also corresponds to one half-wavelength at a BCB-air interface for a free-space wavelength of 10.6 μm [43]. The dipole antenna and CPS widths are 100 nm and 260 nm, respectively.

The separation of the antenna elements determines both the width and location of the maxima in the angular-response pattern. Although the angular resolution improves as the antenna separation increases, the secondary maxima increase in magnitude as they shift towards small angles [38]. Therefore, the antenna separation is chosen to simultaneously optimize the angular resolution while minimizing the magnitude of the side lobes. From a parametric analysis in

HFSS, the optimal separation is $d = 6.45$ µm, consistent with past research for two-element arrays [41].

5.3 Fabrication and Measurement

To investigate the influence of propagation loss on the width of the angular response pattern, two-element phased arrays are fabricated with metal thicknesses of 25 nm/layer and 45 nm/layer. Figure 31 shows the measured and simulated angular response patterns with the incident polarization along the dipole antennas (H-plane). Measured and simulated data are normalized to their maximum values and plotted linear in power to emphasize features of the main lobe in the angular response. For the antenna with increased metal thickness, the full width at half maximum (FWHM) is reduced from 35° to 27°. Such an improvement in angular resolution can be attributed to a reduction in propagation loss as a result of increased confinement of the electric fields between the coplanar strips. As the CPS propagation loss increases, the contribution from the array diminishes and the radiation pattern increasingly resembles the single element pattern. Additional simulations verify that no further beam narrowing is observed for metal thicknesses beyond 45 nm or CPS widths greater than 260 nm.

Figure 31: Measured and simulated angular response patterns in the H-plane of a two-element phased array with a metal thickness of (a) 25 nm/layer and (b) 45 nm/layer.

Figure 32 shows HFSS simulations of the CPS mode distribution for metal thickness of 25nm/layer and 45nm/layer. Clearly, the latter leads to enhanced confinement and increased power density of the CPS mode.
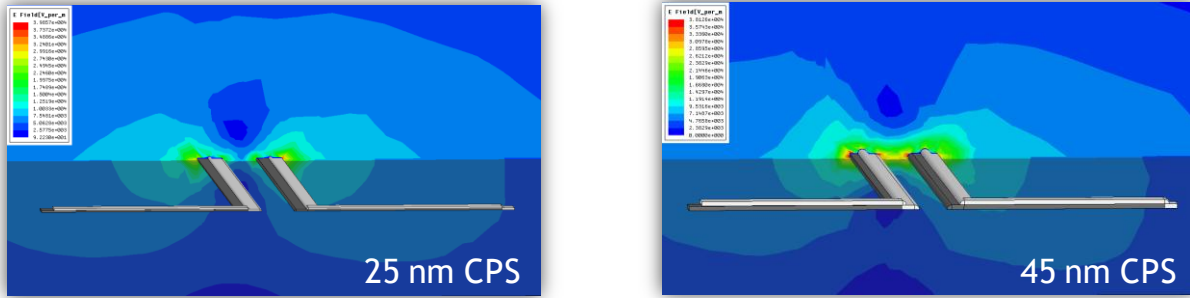
Figure 32: HFSS Simulation of the mode distribution along a CPS for metal different thicknesses.

Values for the attenuation constant α and parameter κ for the two CPS thicknesses can be obtained by performing a least-squares fit between the measured radiation patterns in Figure 31 and Eq. 33. The least-squares fit yields $\kappa = 0.13$ for both cases while the attenuation constant decreases from $\alpha = 0.65$ Np·µm^{-1} for the 25 nm CPS to $\alpha = 0.38$ Np·µm^{-1} for the 45 nm CPS. Although the attenuation constant is reduced by nearly a factor of two from the 25 nm case, the value is still approximately two times greater than previously reported values for CPS transmission lines on BCB in the IR [44].

To demonstrate the effect of additional antenna elements on the angular resolution, one-, two-, four-, and six-element phased-arrays are fabricated on a fixed BCB substrate with 45 nm/layer. Figure 33 shows the measured and simulated angular response patterns in the H-plane. In all cases, there is excellent agreement between simulation and measurement. As the number of antenna elements increases, the angular resolution improves from 120° FWHM for a single dipole to 27° for a two-element array, 21° for a four-element array, and 19.5° for a six-element

array. No further beam narrowing is observed beyond the six-element array due to propagation loss in the CPS.
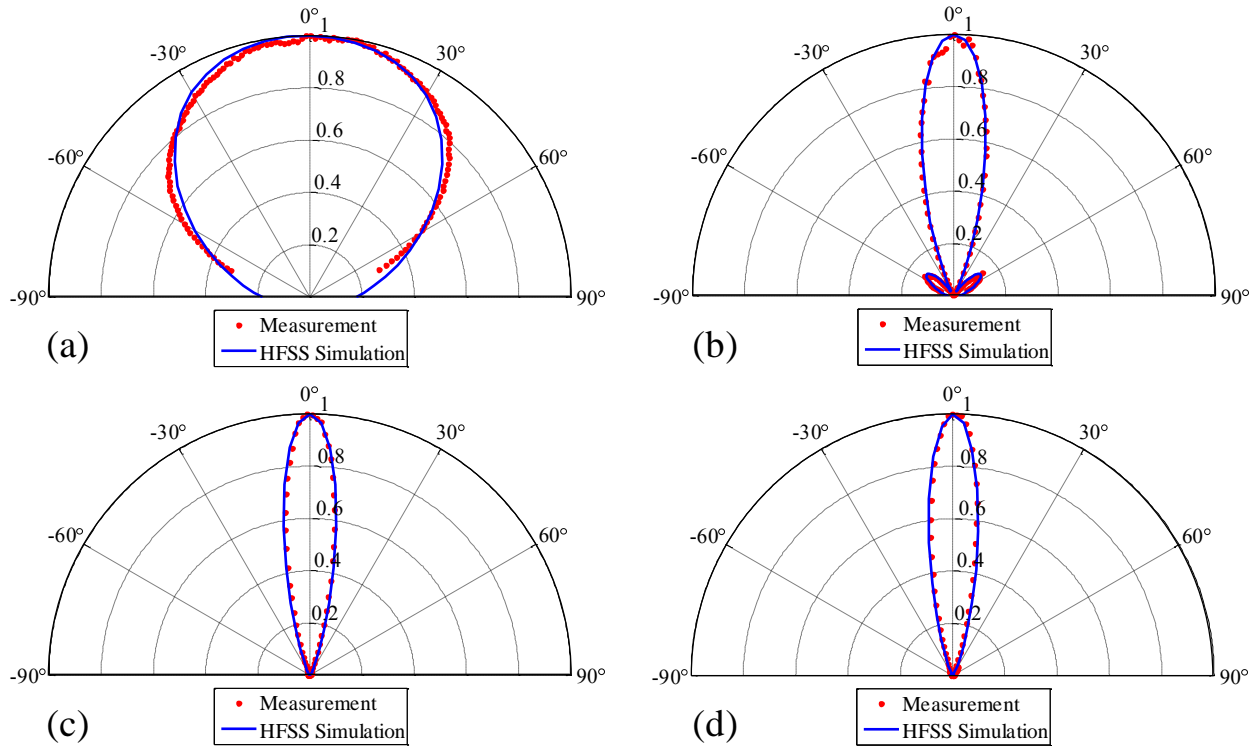
Figure 33: Measured and simulated angular response patterns in the H-plane of (a) a single dipole antenna, and (b) two-, (c) four- and (d) six-element phased-array antennas.

From diffraction theory, the FWHM of an N-element array of equal-amplitude point sources varies as $\lambda_0/(2Nd)$, where d is defined in Figure 30 [8]. Although the measured FWHM for a two-element array is quite close to the expected value, propagation loss leads to a significant amplitude taper for the four- and six-element arrays, with less beam narrowing than would be expected for equal-amplitude arrays, but lower sidelobe levels as well. Simulations indicate that the E-plane response for all arrays closely resembles the E-plane response for a single dipole at a BCB-air interface.

As before, one can determine the CPS attenuation constant by performing a least-squares fit between the measured radiation patterns in Figure 33 and Eq. (33) for multiple-element

phased arrays. When the calculation is carried out, we find that $\kappa = 0.13$ and $\alpha = 0.39$ Np·µm⁻¹, in agreement with the values obtained for the two-element array.

We now proceed to compare the off-broadside angular performance of multiple-element phased-arrays with 45 nm/layer to current state-of-the-art two-element devices with 25 nm/layer. To do so, we fabricate a four-element array with 45 nm/layer and the diode shifted by 1.5 µm and a two-element array with 25 nm/layer and the diode shifted by 0.9 µm. The diode shifts are determined from a parametric analysis in HFSS to achieve the same reception angle of 15° for both antennas [41]. A four-element phased-array is chosen for its simplicity of design and nearly equivalent performance to the six-element array. Figure 34 shows the measured and simulated H-plane angular response patterns. Substantial beam narrowing is observed for the four-element array with thicker metal. The FWHM is reduced from 38° to 21°. Here, the narrowing of the radiation pattern is due to both the additional antenna elements as well as reduced propagation loss in the CPS from the increased metal thickness.
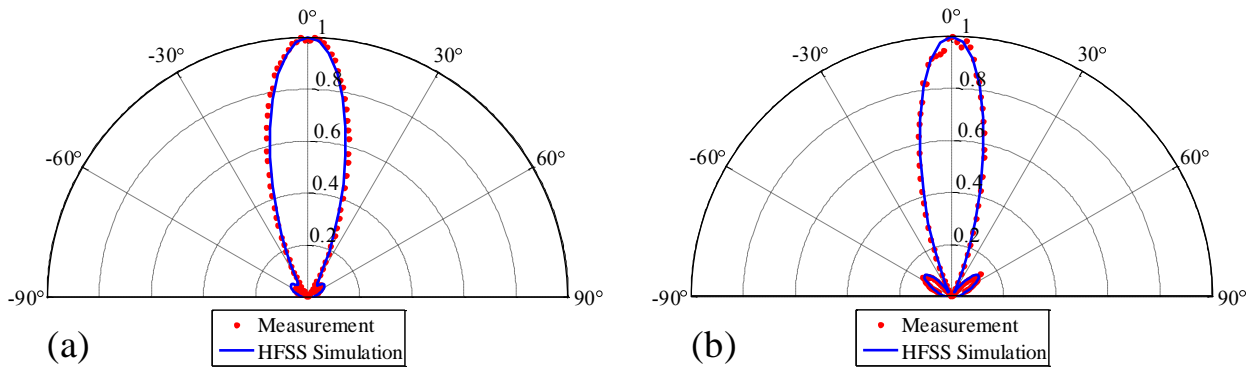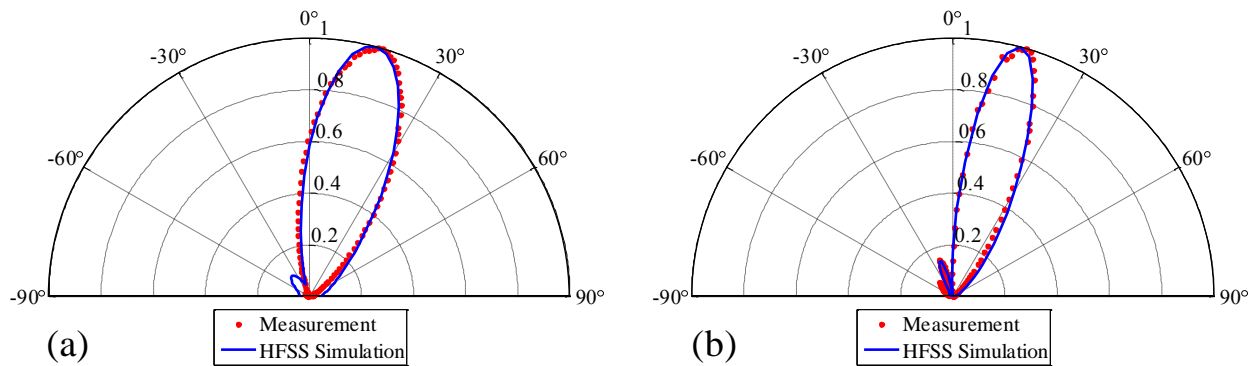

Figure 34: Measured and simulated angular response patterns in the H-plane of a (a) two-element array with 25 nm/layer and 0.9 µm diode shift and (b) four-element array with 45 nm/layer and 1.5 µm diode shift.

5.4 Summary

The angular resolution of a two-dipole phased-array antenna is determined by the separation of the antenna elements. Although improvement in angular resolution is possible by increasing the antenna separation, the emergence of grating lobes into the angular response prohibits the array from operating as a high-resolution, unidirectional receiver. By increasing the number of antenna elements while keeping the separation fixed, the effective antenna aperture can be made larger, and the angular resolution narrower, without introducing grating lobes into the angular response. Measured and simulated angular response patterns at 10.6 μm demonstrate considerable improvement with a four-element array and moderate improvement with a six-element array, the latter attributed to propagation loss in the CPS transmission line that connects the antenna elements. Additional measurements of a two-element array with increased metal thickness indicate that further improvement in angular resolution is possible by reducing propagation loss in the transmission line. In addition, substantial improvement in off-broadside angular resolution is observed with a four-element array, thus motivating the use of multiple-element IR phased-arrays for rudimentary lensless-imaging applications.

CHAPTER 6: SPATIAL-COHERENCE MEASUREMENT

In analogy with a Michelson stellar interferometer, a two-element phased array can be used to assess the degree of coherence of a partially coherent field, and through the Van Cittert-Zernike theorem, deduce the spatial intensity distribution of the source [45]. This approach has been implemented at microwave frequencies by radio astronomers since the 1950s. Image reconstruction of astronomical sources is achieved via inverse Fourier transformation of the complex electric fields measured at spatially separated observatories [46]. Methods of measuring the coherence function in the IR include intensity interferometry with heterodyne detection [47], IR-to-visible up conversion interferometry [48], and antenna-coupled microbolometric detection [49]. The latter approach is inherently limited by the distributed impedance that is characteristic of bolometers with poor TCR contrast [2]. Moreover, previous configurations had the antenna geometry fixed while varying the diameter of the spatially incoherent source.

We present a method in which the spatially incoherent source is fixed while the separation of the antenna elements is varied [50]. In this configuration, the degree of spatial coherence is a measure of the correlation of electric fields received by the antennas as a function of their separation. This scheme is analogous to Young's double-slit arrangement with the pinholes replaced by dipole antennas and the far-field transformation of light from the pinholes to the observation screen regarded as propagation of antenna currents along a CPS transmission line.

65

6.1 Method

The traditional setup for measuring the degree of coherence of a partially coherent field consists of a pair of pinholes and an observation screen [45]. For a two-element phased array, the separation of the dipole antennas is analogous to the pinhole separation and the MOM diode represents a point on-axis in the observation screen. Figure 35 contains electron micrographs of the two-element phased-array antenna and MOM diode. The dipole antennas are separated by a distance L and the MOM diode is located at the center of the array.
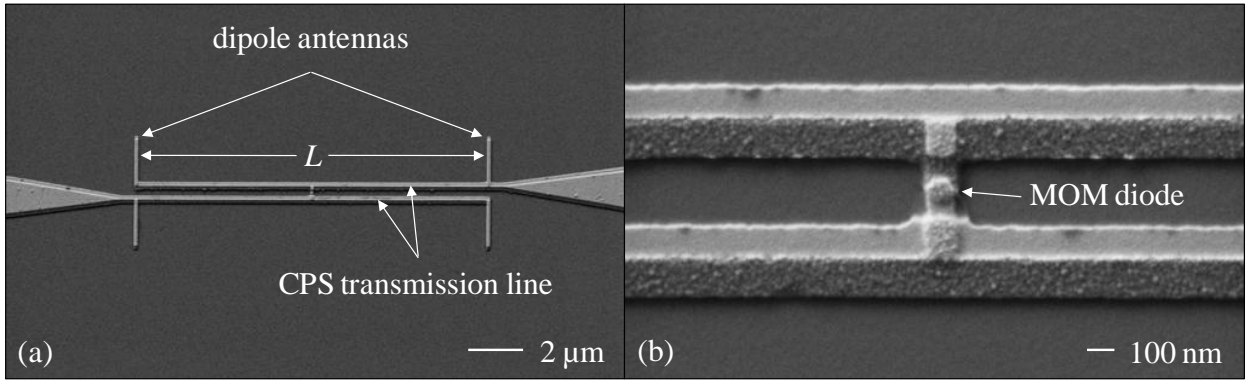
Figure 35: Electron micrographs of the phased-array antenna (a) and MOM diode (b).

With CPS propagation loss included, the two-source interference law for partially coherent light is [45]

$$I(L) = \exp(-\alpha L)[I_1 + I_2 + 2\sqrt{I_1 I_2} \operatorname{Re} \gamma(L)], \qquad (34)$$

where I_1 and I_2 are the squares of the CPS current amplitudes, α is the attenuation constant of the CPS, and $\gamma(L)$ is the complex coherence function of the partially coherent source. Consider a circular lens uniformly illuminated with monochromatic spatially incoherent light. From the Van Cittert-Zernike theorem, the coherence function on-axis is real with a magnitude [51]

$$|\gamma(L)| = 2 \left| \frac{J_1(\pi L / \lambda F / \#)}{(\pi L / \lambda F / \#)} \right|, \qquad (35)$$

66

where $F/\#$ is the focal ratio of the lens, λ is the wavelength, and $J_1(x)$ is a Bessel function of the first kind. If the CPS currents have equal magnitudes, $I_1 = I_2 = I_0$ and Eq. (34) simplifies to

$$I(L) = 2I_0 \exp(-\alpha L)[1 + |\gamma(L)|].$$ (36)

Eq. (36) represents the measured antenna response, which is generally subject to device non-uniformity through the parameter I_0. Determination of the coherence function from Eq. (36) thus requires knowledge of the CPS attenuation constant and device uniformity. Therefore, a calibration method is required for extraction of the coherence function from the measured response. To this end, consider the antenna response under coherent illumination with $\gamma(L)=1$,

$$I_C(L) = 4I_{0,C} \exp(-\alpha L),$$ (37)

where the letter C denotes coherent illumination. For partially coherent illumination (denoted by the letter P), the coherence function can take any value between zero and unity,

$$I_P(L) = 2I_{0,P} \exp(-\alpha L)[1 + |\gamma(L)|].$$ (38)

By eliminating the exponential with Eq. (37), we can solve for the coherence function in Eq. (33) to obtain

$$|\gamma(L)| = 2\frac{I_{0,C}I_P(L)}{I_{0,P}I_C(L)} - 1.$$ (39)

The ratio $I_{0,C}/I_{0,P}$ can be determined by measuring the single dipole response ($L = 0$) under coherent and partially coherent illumination ($I_C(0)$ and $I_P(0)$, respectively). Taking the ratio of these quantities yields

$$\frac{I_C(0)}{I_P(0)} = \frac{2I_{0,C}}{I_{0,P}[1 + \gamma(0)]} = \frac{2I_{0,C}}{I_{0,P}[1+1]} = \frac{I_{0,C}}{I_{0,P}}.$$ (40)

Inserting the ratio from Eq. (40) into Eq. (39), the coherence function can be written as

$$|\gamma(L)| = 2\frac{I_C(0)I_P(L)}{I_P(0)I_C(L)} - 1. \tag{41}$$

To verify that the quantity in Eq. (41) is independent of device non-uniformity, first consider the ratio $I_C(0)/I_P(0)$. Since the electric fields are perfectly correlated at the location of a single dipole, the ratio $I_C(0)/I_P(0)$ is simply a measure of the power ratio of the two sources. Now, the quantity $I_P(L)/I_C(L)$ depends on the power ratio of the sources as well as the degree of coherence at the antenna separation L. Therefore, their combined ratio in Eq. (36) can depend only on the degree of coherence. To summarize, by measuring the responses of a single dipole and two-element phased-array under coherent and partially coherent illumination, the coherence function can be determined independently of propagation loss and device non-uniformity. In this calibration method, we are effectively equating the device responses for coherent illumination.

6.2 Simulation and Design

When excited with infrared radiation, MOM diodes exhibit a non-linear *I-V* characteristic caused by the tunneling of electrons through the insulator layer [9]. At zero bias, the dc component of the rectified current is proportional to the optical power dissipated in the oxide layer [7]. In HFSS, a quantity proportional to the rectified current is computed as the power loss density integrated over the aluminum-oxide volume [39]. From Eq. (41), the degree of coherence can be calculated by evaluating the antenna response for coherent and partially coherent illumination. To simulate coherent F/8 illumination (see section 6.4) for determination of $I_C(L)$, the antenna is excited in HFSS with a Gaussian beam of waist $w_0 = 115$ µm and wavelength 10.6 µm (28.3 THz). The power dissipated in the oxide layer is then calculated as a function of the antenna separation. For the partially coherent case, we calculate the power dissipated for F/1

Gaussian beam illumination at each angle of incidence in an $F/1$ cone (54° full angle) and evaluate the sum to obtaine $I_P(L)$. In this respect, by applying the principle of superposition of powers (or intensities), we are assuming a spatially incoherent source. The coherence function is calculated by taking the ratio of the coherent and partially coherent responses in the manner prescribed by Eq. (41).

Design considerations for a two-element phased array include the substrate configuration, antenna length and spacing, and CPS gap width. To reduce inhomogeneities in the dielectric environment and hence reduce propagation loss in the CPS, the devices are fabricated on a low-index ($n = 1.55$) quarter-wavelength dielectric layer above a ground plane [31, 35]. The dielectric is a 1.7 μm layer of benzocyclobutene (BCB), a low-loss insulator ($k = 0.015$) at 10.6 μm. The antenna length and CPS separation are chosen to optimize power transfer from free-space radiation to confined modes in the CPS [42]. From a parametric analysis, the optimal antenna length and CPS gap width are 4 μm and 470 nm center-to-center, respectively. This antenna length corresponds to one half-wavelength of 10.6 μm radiation at a BCB-air interface [43]. The dipole antenna and CPS widths are 100 nm and 260 nm, respectively. The maximum antenna separation is chosen to minimize propagation loss in the CPS and to include the first zero of the coherence function, which from Eq. (35), occurs for an antenna spacing

$$L_0 = 1.22\lambda F/\#. \tag{9}$$

A recent investigation of the influence of propagation loss on the angular response patterns of multiple-element IR phased arrays demonstrates that antenna elements with separations greater than 24 μm do not contribute to the measured response [39]. Anticipating a similar degree of propagation loss and with knowledge of the condition for minimum visibility,

we choose an $F/1$ spatially incoherent source and vary the antenna separation between zero and 18 µm.

6.3 Measurement

An illustration of the measurement configuration is shown in Figure 36. A 10.6 µm CO_2 laser is mechanically chopped at 1.5 kHz in the focal plane of a ZnSe lens. The diverging radiation is passed through a rotating piece of sandblasted BaF2 and focused by an $F/1$ BaF_2 lens placed directly behind the diffuser. In this configuration, the Fraunhofer diffraction pattern of the spatially incoherent field is generated in the focal plane of the $F/1$ lens [52].
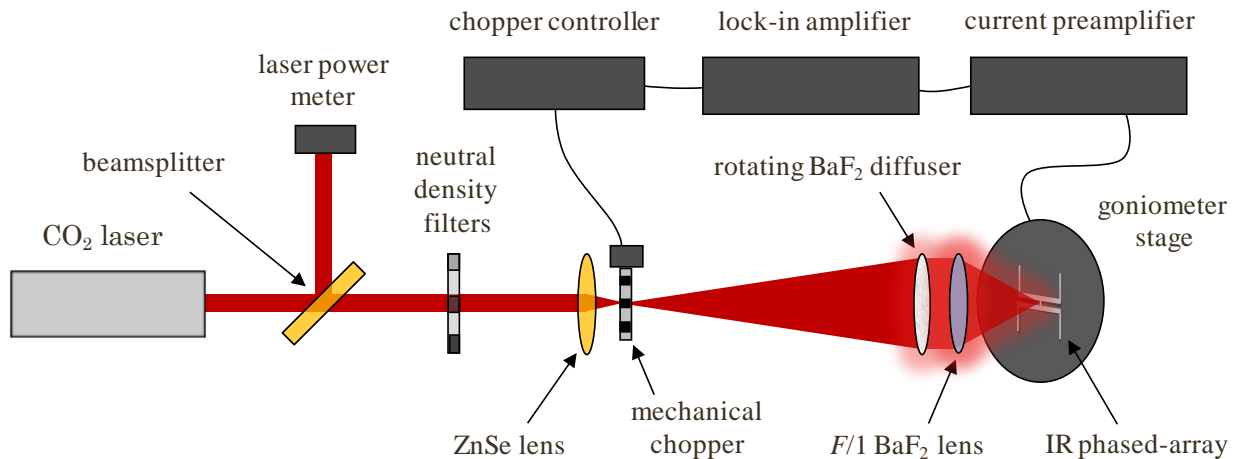
Figure 36: Experimental configuration for spatial coherence measurements. Radiation passing through the BaF_2 diffuser undergoes diffuse refraction to form a spatially incoherent field. The Fraunhofer diffraction pattern is generated in the focal plane of the $F/1$ lens. For calibration, the diffuser and $F/1$ lens are replaced with a collimating lens and $F/8$ objective, respectively.

The phased-array antenna is mounted to a five-axis goniometer located in the focal plane of the $F/1$ lens [17]. The rectified current from the MOM diode is passed through an external current preamplifier and monitored with a lock-in amplifier that is referenced to the frequency of the mechanical chopper. Temporal fluctuations in the laser power are accounted for by

normalizing the measured current to the reference power. Measurements are conducted without external applied bias and with a laser irradiance of approximately 10 W·cm^{-2}. The measured response to radiation polarized perpendicular to the dipoles is nearly equal to the Johnson noise, which indicates that the dc lead line and thermal contributions are negligible.

One can characterize the coherence properties of the diffuser by comparing the surface roughness to the average displacement of the diffuser between consecutive measurements. For example, if the chopper frequency is 1.5 kHz and the average diffuser rotational frequency is 3 Hz, there are 500 measurements during one rotational cycle of the diffuser. The displacement between measurements by a point midway between the center and edge of a 5 cm diameter diffuser is approximately $0.5\pi(5 \text{ cm})/500 \approx 160$ µm. From contact profilometry measurements of the BaF$_2$ surface, depth variations of 1-2 λ are separated on average by 10 λ, or around 100 µm. Since the average roughness separation is less than the displacement between measurements, the phase distribution across the diffuser can be regarded as random between measurement cycles, thus substantiating the use of a spatially incoherent source in the simulations.

Figure 37 shows the diffuser, F/1 transform lens and phased-array antenna. The diffuser is connected to three pulleys, with the top pulley connected to an electric motor. The motor is connected to an external dc power supply. The F/1 transform lens is nearly in contact with the diffuser.

Determination of the coherence function from Eq. (41) requires measurement of the coherent and partially coherent responses. For the coherent response $I_C(L)$, each device is measured under F/8 illumination with the diffuser removed. A high F/# lens is less susceptible to alignment errors and generates a large spot size compared to the antenna separation. The latter

condition is essential when comparisons are made to the extended uniform image of a partially coherent source. The F/8 optics are then removed and replaced by the diffuser and F/1 transform lens. The antenna response is then measured to obtain $I_P(L)$. From Eq. (41), the coherence function is calculated by normalizing to the single dipole ratio $I_C(0)/I_P(0)$.
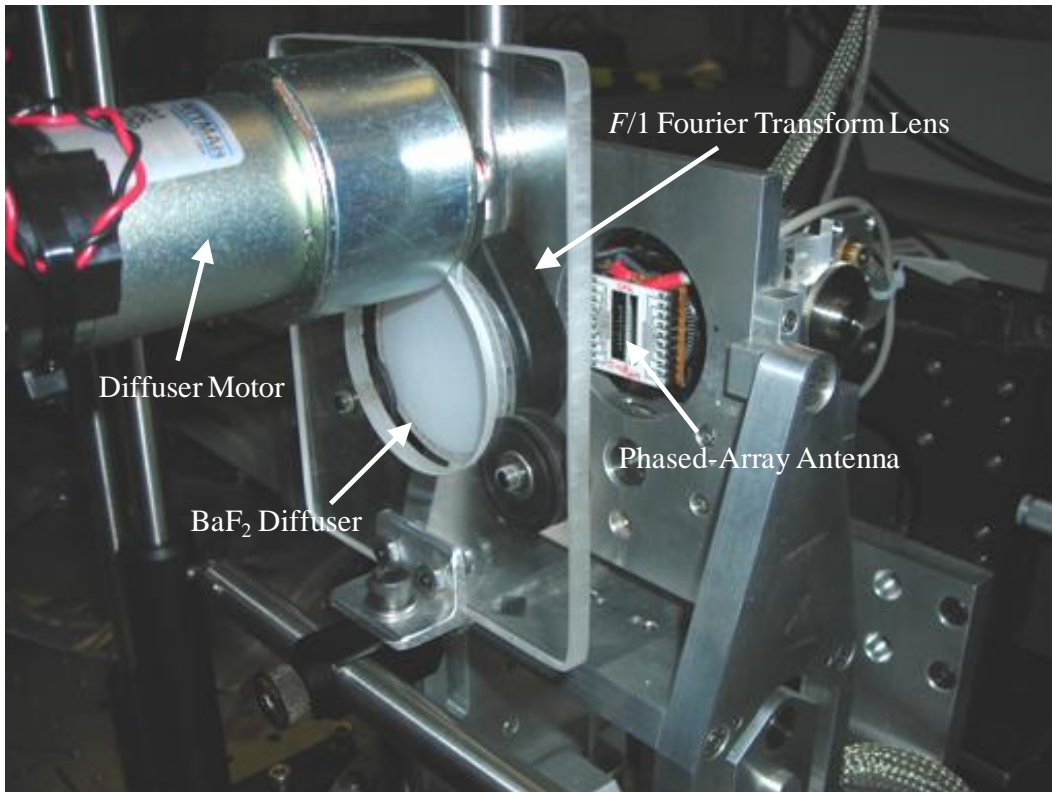
Figure 37: Rotating Diffuser and F/1 Fourier transform lens.

Figure 38 shows the measured coherence function compared with the HFSS simulation and analytical result from the Van Cittert-Zernike theorem for a spatially incoherent uniformly illuminated disk (Eq. (35)). Error bars represent one standard deviation from the mean of measurements conducted with diffuser frequencies of 1.5, 3, 4.5, and 6 Hz. Agreement between simulation and measurement is very good, while moderate discrepancies are apparent between the measurement and the Van Cittert-Zernike result. In all three cases, the minimum in the

coherence function occurs for antenna separations between 12-13 μm, in agreement with Eq. (35). For this antenna separation, the electrics fields received by the antennas are uncorrelated in the sense that CPS current amplitudes generated by these antennas will not exhibit interference. Instead, the principle of superposition applies to the CPS current intensities. Deviations from the Van Cittert-Zernike theorem, including the oscillations at large antenna separations, are attributed to mutual interactions between the reradiated fields of the dipole antennas and variations in the effective impedance of the CPS as a function of the antenna separation. Both effects are apparent in simulations as deviations from the exponential behavior predicted by Eq. (37). If the aluminum-oxide layer is replaced with a different material (e.g., SiO_2), the oscillations in the simulated coherence function shift spatially, inferring that these features are related to an impedance mismatch between the CPS and diode.
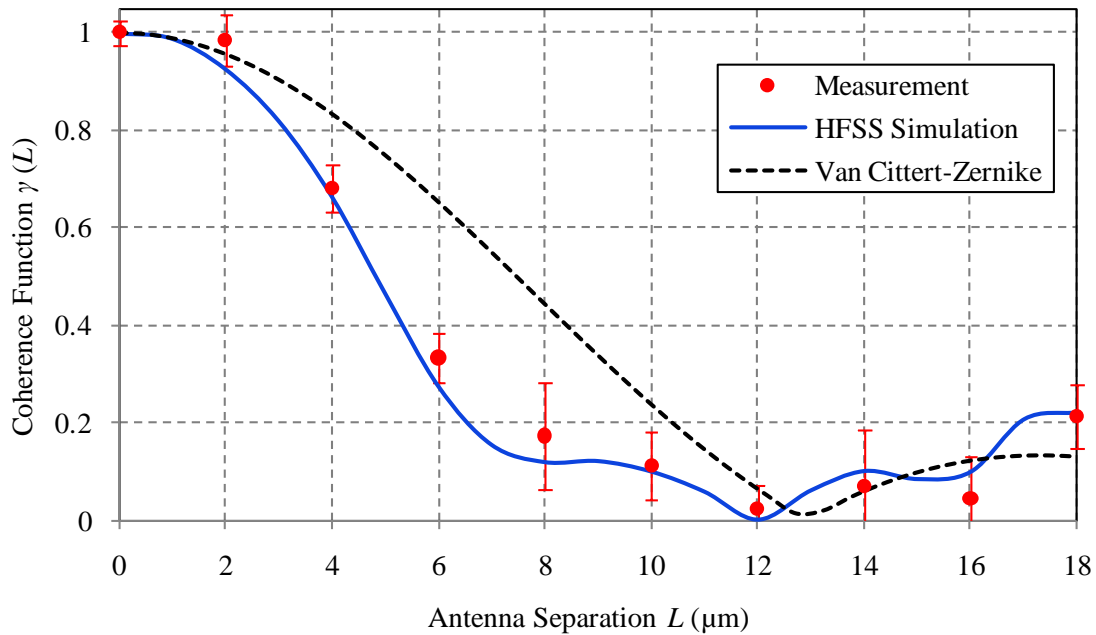
Figure 38: Measured and simulated spatial coherence function versus antenna separation for a two-element phased-array. The standard result from the Van Cittert-Zernike theorem is also shown.

Fortunately, the loss of coherence for large antenna separations lends itself to a simple geometric interpretation. To see this, consider the illustration in Figure 39. Because of diffraction, the width of the angular response pattern narrows as the separation of the antenna elements increases. For coherent illumination, the rays exiting the F/1 lens undergo diffraction to generate a Gaussian beam. In this case, the rays in the focal plane of the F/1 lens are approximately collimated. Therefore, the detector response is determined by rays originating near the optical axis of the source. Since the radiation pattern near broadside is essentially unchanged as the antenna separation increases, there is no reduction in measured response for coherent illumination.
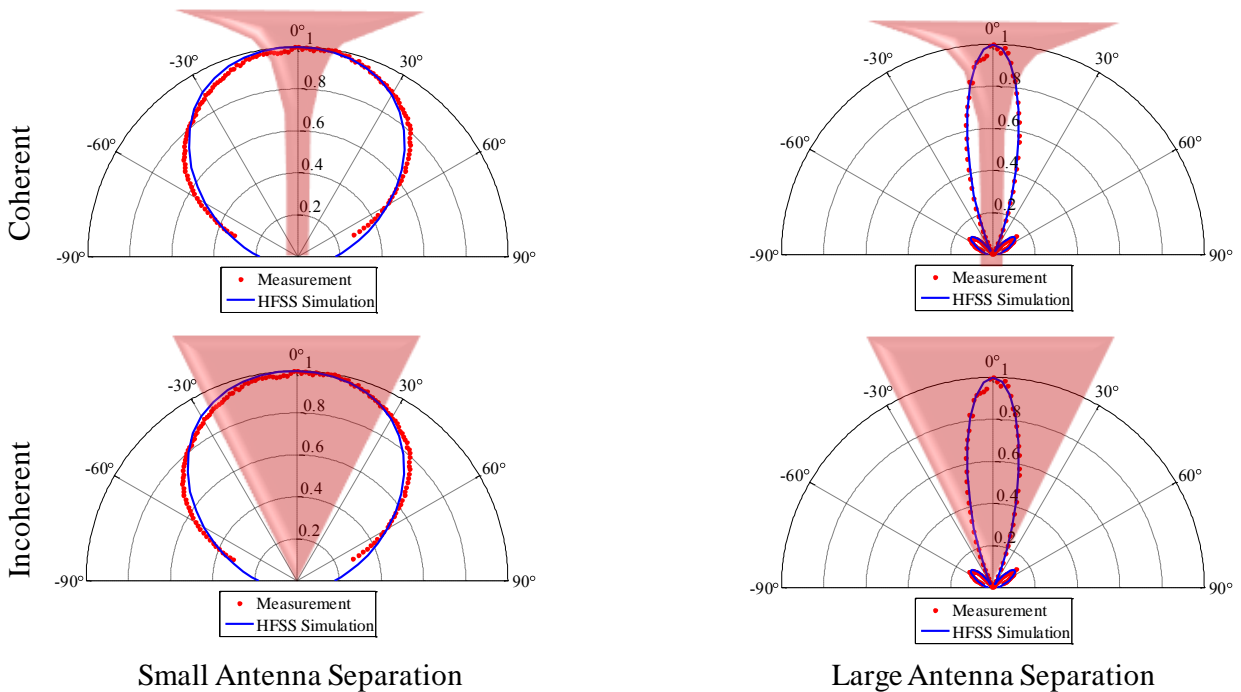
Figure 39: Geometric interpretation of coherence loss with increasing antenna separation.

For partially coherent illumination, the amount of diffraction is limited. As a result, over time the detector will respond to rays originating from all points on the source, not only those

originating near the optical axis. As the antenna separation increases, the contribution from large angles decreases since the angular response pattern narrows. Therefore, integration over the source cone angle leads to a diminished response for large antenna separations. This effect does not occur when the radiation is coherent because the rays are approximately collimated near focus.

6.4 Summary

In analogy to Young's double-slit experiment, a phased-array antenna can be used to assess the degree of coherence of a spatially extended monochromatic optical field. For a two-element array, the degree of coherence is a measure of the correlation of electric fields received by the antennas as a function of the element separation. In general, phased-array antennas coupled to MOM diodes and CPS transmission lines are subject to propagation loss and device non uniformity. By properly calibrating the antenna response with coherent illumination and normalizing with respect to the single-dipole response, the coherence function can be extracted from the measured antenna response under partially coherent illumination. Measurements are conducted using a rotating piece of sandblasted BaF_2. An F/1 Fourier transform lens is placed directly behind the diffuser so that the Fraunhofer diffraction pattern is formed in the focal plane of the lens. In this configuration, the antenna response is simply the integration of the antenna response over the cone angle of the lens. Electromagnetic simulations and the analytical result from the Van Cittert-Zernike theorem are confirmed by measurements with a 10.6 μm CO_2 laser and a partially coherent *F*/1 source.

CHAPTER 7: FUTURE WORK

Future work would potentially include a continuous-wavelength responsivity measurement of diode amplitude arrays, temporal coherence measurements, and tunable phased-array antennas using the thermochromic properties of VO_2.

7.1 Continuous-Wavelength Responsivity Measurement

One of the primary motivations for separating the radiation sensor from the receiver is to allow polarization and wavelength control with the antenna geometry. Although the response of IR antenna-coupled detectors has been measured as a function of antenna length [13], the wavelength response has only been measured at discrete laser lines [53]. It would be beneficial to acquire a continuous wavelength scan using, for example, a variable-angle prism spectrometer. The prism spectrometer consists of a filament source and variable-angle Thallium Bromoiodide (KRS-5) prism, as shown in Figure 40. By varying the angle of the prism, the dispersed spectrum of light can be moved across a device placed at the focus of the output mirror. Unfortunately, a continuous wavelength scan has never been conducted in the past due to the low irradiance of the spectrometer source and insufficient device SNR.

One way to increase SNR is to form an array of diodes [54]. In contrast with a phased-array antenna, this device would operate as an amplitude-only detector. Since each diode acts a dc current source, the rectified currents will add when the diodes are connected in parallel, as shown in Figure 40.

These devices are fabricated on a 500 nm layer of ZnS above a ground plane. This material was chosen for its low absorption in the $8-12$ μm band. The ground plane leads to enhanced fields in the substrate and thus to a narrower resonance as a function of antenna length. Since the filament source in the prism spectrometer is randomly polarized, a cross dipole design is used to capture all incident polarizations.

Prism Spectrometer   *Parallel Diode Array*
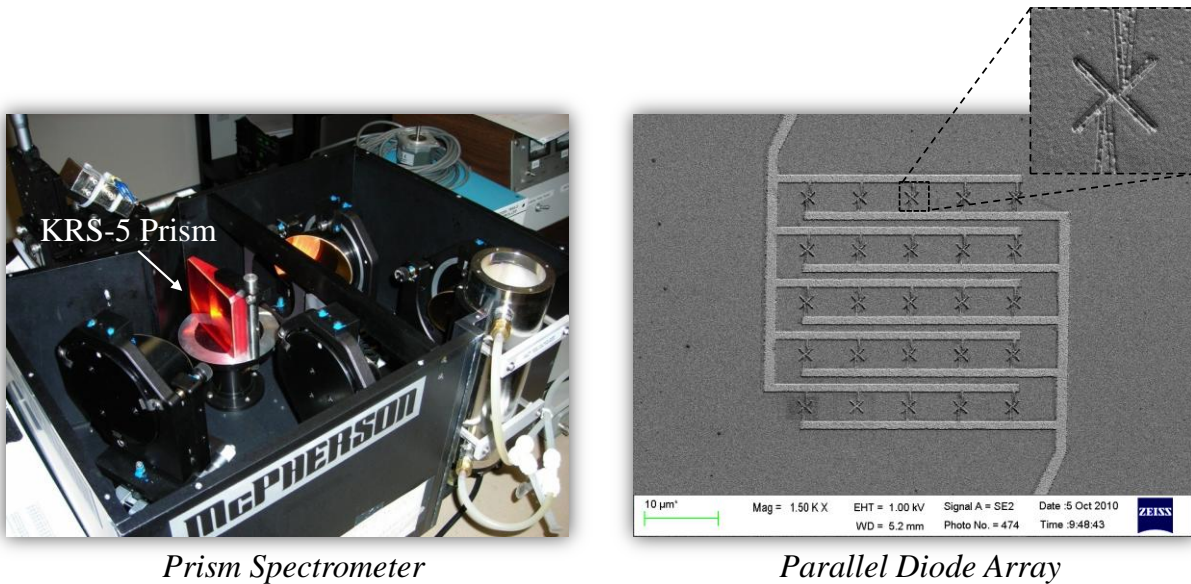
Figure 40: Diode arrays for continuous-wavelength responsivity measurement. Diodes are connected in parallel so that their rectified currents add.

To verify the spectral response of the cross dipole design, the device response was measured with the tunable-grating CO_2 laser. The results are shown in Figure 41. The measurements are normalized to the reference power of the laser. There is general agreement between simulation and measurement on the resonance wavelength of 10.3 μm. However, the bandwidth of the measured response is narrower than the prediction. In future simulations, the lead-line structure in Figure 40 will be included to obtain more accurate simulations.
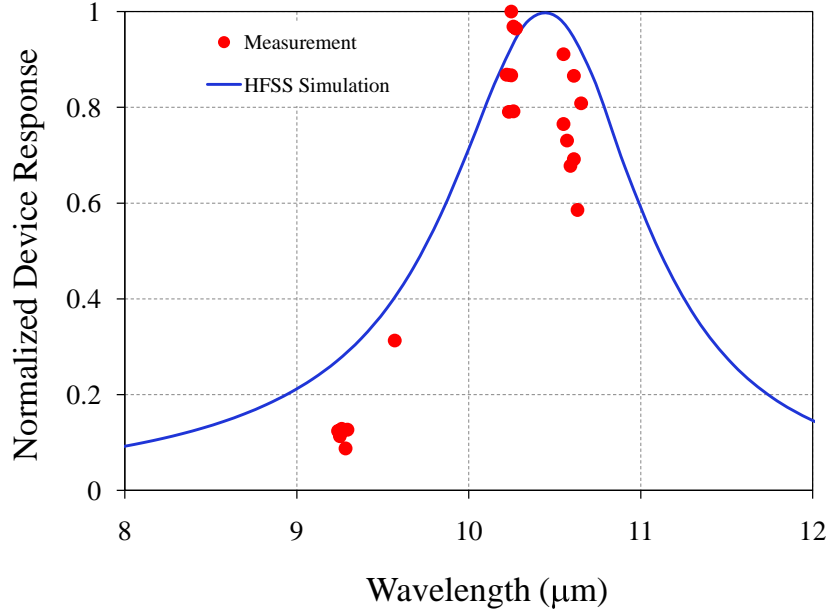
Figure 41: Wavelengh response of the diode array in Fig. 25 measured with a grating-tunable CO_2 laser.

7.2 Temporal Coherence Measurements

By analogy with a Michelson interferometer, the two-element phased-array can be used to measure the temporal degree of coherence of a polychromatic source. To see this, consider the interference law for a two-element phased-array illuminated at broadside with monochromatic light

$$I(k,\Delta) = 2I_0[1+\cos(2kn\Delta)] \tag{42}$$

where $2n\Delta$ is the optical path length introduced by the diode shift. If the source is polychromatic and described by a spectrum $S(k)$, the measured response will be the integration of Eq. (42) over the spectrum,

$$I(\Delta) = C\int_{-\infty}^{\infty}I(k)S(k)dk = C2I_0\left[\int_{-\infty}^{\infty}S(k)dk + \int_{-\infty}^{\infty}S(k)\cos(2kn\Delta)dk\right] \tag{43}$$

where C is a proportionality constant. If the first integral in Eq. (43) is normalized to C^{-1}, the measured response can be written as

$$I(\Delta) = 2I_0[1 + \phi(\Delta)], \tag{44}$$

where

$$\phi(\Delta) = C \int_{-\infty}^{\infty} S(k)\cos(2kn\Delta)dk . \tag{45}$$

Therefore, $\phi(\Delta)$ is the real Fourier transform, or auto-correlation, of $S(k)$. The spectrum of the source is then calculated as the inverse Fourier transform of $\phi(\Delta)$ as

$$S(k) = \frac{1}{2\pi C} \int_{-\infty}^{\infty} \phi(\Delta)\cos(2kn\Delta)d\Delta . \tag{46}$$

Therefore, the spectral distribution of the source can be determined by taking the auto-correlation of the phased-array response as a function of the diode shift. A simple would consist of two laser lines, in which case, the measured response would be proportional to a product of cosine functions evaluated at the sum and difference frequencies. To eliminate device non-uniformity and propagation loss, a calibration procedure similar to that used for the spatial coherence measurements would be required.

7.3 Tunable Phased-Array Antennas

For certain applications, it may be necessary to dynamically tune the angular response of a phased-array antenna. This may be possible with the recent discovery of the thermochromic properties of vanadium dioxide (VO_2) in the IR [55]. VO_2 exhibits a temperature-dependent refractive index. As the temperature increases from 20°C to 70°C, the refractive index varies from 1.84 to 5.84 and the absorption constant changes from 1.04 to 2.72. Following the

discussion in Chapter 4, one can introduce an inter-element phase shift by inserting a VO_2 element directly between the coplanar strips, as shown in Figure 42.
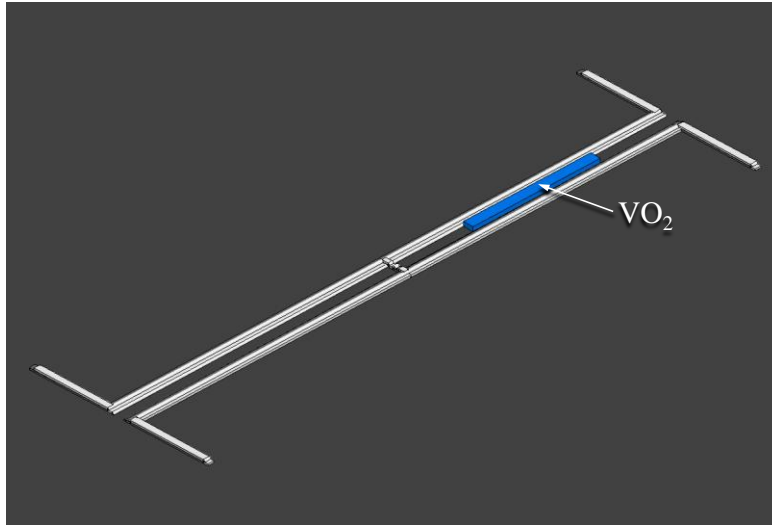
Figure 42: Two-element phased array with VO_2 phase-shifting element.

With the VO_2 properties set to those at 70°C, a parametric analysis is performed in HFSS to determine the optimal length for the VO_2 element. The optimal length yields the largest response angle with an acceptable side-lobe level. Figure 43 shows the simulated angular response patterns for the tunable phased-array. As the VO_2 temperature increases from 20°C to 70°C, the response angle varies from 0° to 7°. Although larger response angles are attainable by increasing the length of the VO_2 element, the side-lobe level increases substantially.
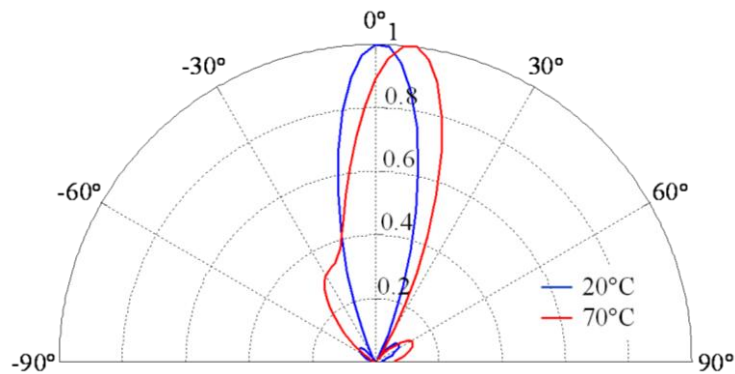
Figure 43: Simulated angular response patterns for a tunable VO_2 phased-array antenna.

CHAPTER 8: CONCLUSIONS

Infrared dipole antenna-coupled metal-oxide-metal diodes provide a unique detection mechanism that allows for determination of the polarization and wavelength of an optical field. By measuring the response of several dipole antennas with various lengths and orientations, one can determine the polarization and wavelength of the incident radiation. This device concept is illustrated in Figure 44. We can extend this concept further to include phased-array antennas in order to determine the angle of arrival and degree of coherence of received IR radiation. In this configuration, one can potentially determine the polarization, wavelength, angle of arrival, and degree of coherence all from a single chip.
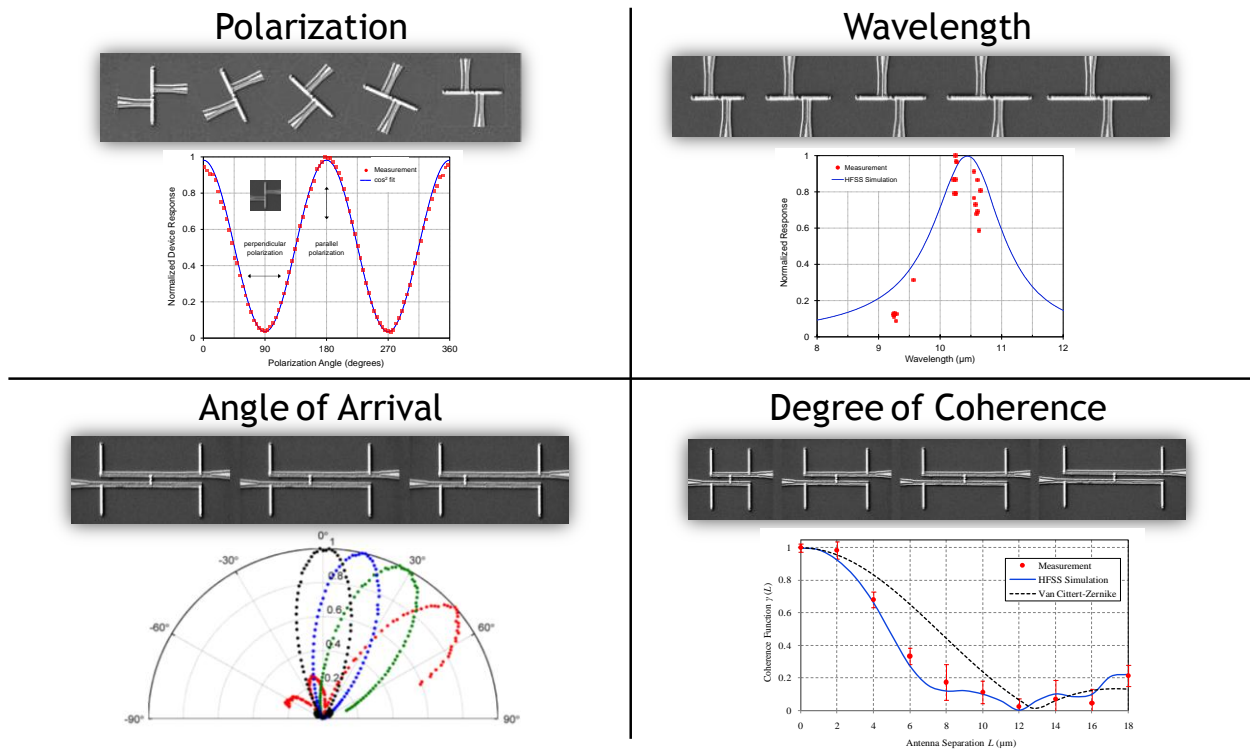
Figure 44: Device concept for determination of polarization, wavelength, angle of arrival, and degree of coherence.

The angular response characteristics of IR dipole antennas are determined by boundary conditions imposed by the surrounding dielectric or conductive environment on the electromagnetic fields in the vicinity of the device. We investigated several substrate configurations, including both planar and hemispherical lens substrates. Measurements at 10.6 μm demonstrate that the angular response can be tailored by the thickness of the electrical isolation stand-off layer on which the detector is fabricated and/or the inclusion of a ground plane.

Directional detection of IR radiation is achieved with a pair of dipole antennas coupled to a MOM diode through a coplanar strip transmission line. The direction of maximum angular response is altered by varying the position of the diode along the transmission line connecting the antenna elements. By fabricating the devices on a quarter-wavelength layer above a ground plane, narrow beam widths of 35° full width at half maximum and reception angles of ± 50° are achievable with side lobe contributions less than 25%.

Although the two-element phased-array is capable of detecting large angles of arrival, the width of the angular response pattern, or the angular resolution, is determined by separation of the antenna elements, which is bounded from above by the emergence of grating lobes. To improve this situation, one can increase the number of antenna elements while keeping the antenna separation fixed. This has the effect of increasing the effective aperture of the antenna without introducing grating lobes into the angular response. In addition, the angular resolution can also be improved by reducing propagation loss in the CPS transmission line. One possibility is to increase the confinement of electric fields between the coplanar strips by increasing the

82

metal thickness. This has the effect of reducing the cross sectional area of the mode, and thus increasing its power density.

A two-element phased array antenna can also be used to assess the degree of coherence of a partially coherent source. For a two-element array, the degree of coherence is a measure of the correlation of electric fields received by the antennas as a function of the element separation. In general, the measured antenna response is subject to CPS propagation loss and device-to-device non-uniformity. Therefore, to extract the coherence function from the measured response, a calibration method is required whereby the antenna response to partially coherent illumination is normalized to the device response for coherent laser illumination. Measurements of a spatially incoherent F/1 circular source are corroborated with HFSS simulations and the analytical result from the Van Cittert-Zernike theorem.

APPENDIX A: FABRICATION OF ANTENNA-COUPLED MOM DIODES

Fabrication of infrared antenna-coupled MOM diodes is well documented [13, 14]. The process includes electron beam lithography and a shadow evaporation consisting of two metal depositions and an intermediate oxidation step. Evaporation at two opposing angles generates a small area, typically 80×80 nm, where the two metals overlap beneath a bridge of undercut electron beam resist. The entire antenna structure, including the lead lines, CPS, and diode are metalized during a single shadow evaporation. MOM diodes fabricated using a native oxidation tended to produce diodes with high dc resistance, leading to low device yield and high devce-to-device non-uniformity. By performing a controlled, low pressure oxidation, the barrier thickness can be limited to 1-2 nm.

The resist bilayer consists of approximately 50 nm of PMMA A2 on top of 500 nm of MMA copolymer (EL 11). Both layers are spun on at 4000 rpm for 1 minute and baked for 2 minutes at 180°C. Since the copolymer develops more rapidly than PMMA, resist development generates an isotropic undercut in the MMA layer, as shown in Figure 45. If two developed features are brought close enough together, as shown in Figure 46, the undercut portions of the resist overlap so that no resist remains underneath the suspended bridge of PMMA.
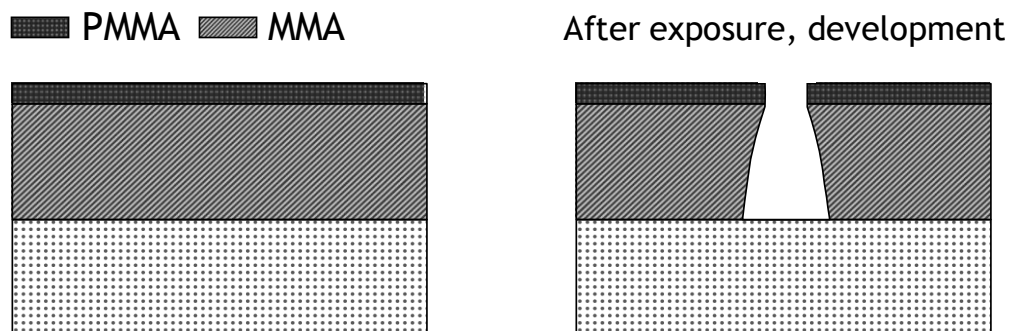
Figure 45: Undercut with resist bilayer.

85
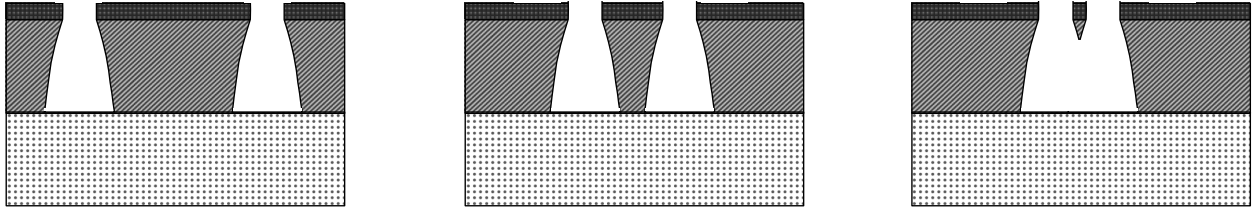
Figure 46: PMMA bridge formation.

The bridge gap dimension in L-Edit should be designed at 70-80 nm. If the gap dimension is too small, the bridge will develop away, typically resulting in a closed circuit. If the gap is too large, the two metals will not overlap during the shadow evaporation, and the *I-V* curve will resemble an open circuit. The antennas and bridge widths are 100 nm. Both are written with an e-beam dose of 500 $\mu C \cdot cm^{-2}$. During the fracture process, we use 5 nm resolution (res 0.005) and 1 nA beam current (beam 0.005). The exposed resist is developed for 1 minute in a 3:1 IPA:MIBK solution. Figure 47 contains an electron micrograph of the developed resist. The resist has been coated with a thin aluminum film to prevent charging under bombardment from the SEM. After development, the PMMA bridge is approximately 80 nm $\times$ 100 nm.
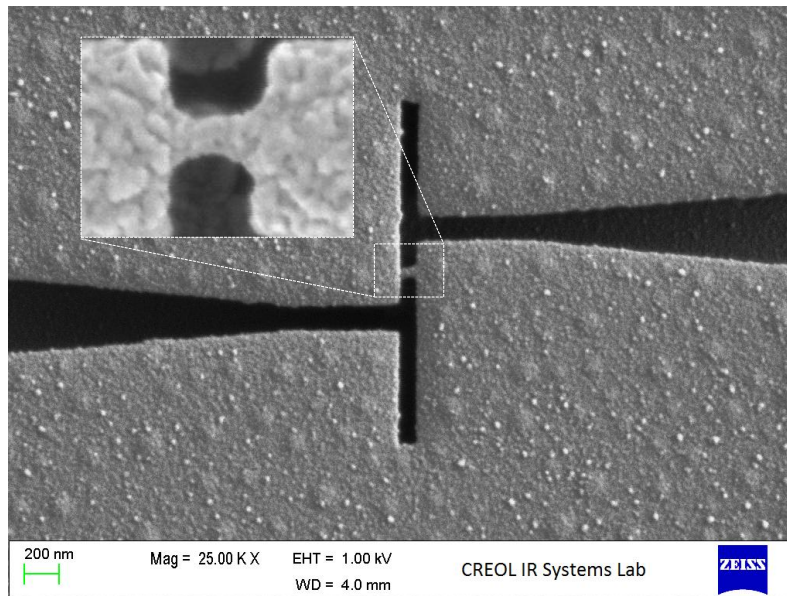
Figure 47: Exposed and developed resist pattern for antenna-coupled MOM diodes.

Following development, the patterned resist is placed in the barrel etcher for a 2 minute O_2 descum at 200 W and 400 mTorr. This process removes residual resist and other organics.

Figure 48 illustrates the three-step shadow evaporation method. First, a 30 nm aluminum layer is deposited at a 7° angle relative to the substrate normal using the custom tilt stage. The chamber is then filled with oxygen gas at a pressure of 50-100 mTorr for 30 minutes to allow a thin 1 - 2 nm layer of aluminum-oxide to form on the aluminum elements. While under vacuum, the substrate stage is switched to a -7° angle and a 30 nm platinum layer is deposited. The MOM diode is located at the overlap area beneath the PMMA bridge. From inspection of Figure 48, one finds that the only path for electrical current is through the MOM diode.

Figure 48: Shadow evaporation method for MOM diode fabrication.

Prior to the depositions, ensure that the O_2 lines are plugged into the mass flow controller and that the "ion N_2" valve is open. The latter prevents a gas surge during the metallization.

Mount the antennas on the tilt stage with the antenna axis parallel to the direction of the tilt arm. Use Kapton tape to hold the devices to the tilt stage and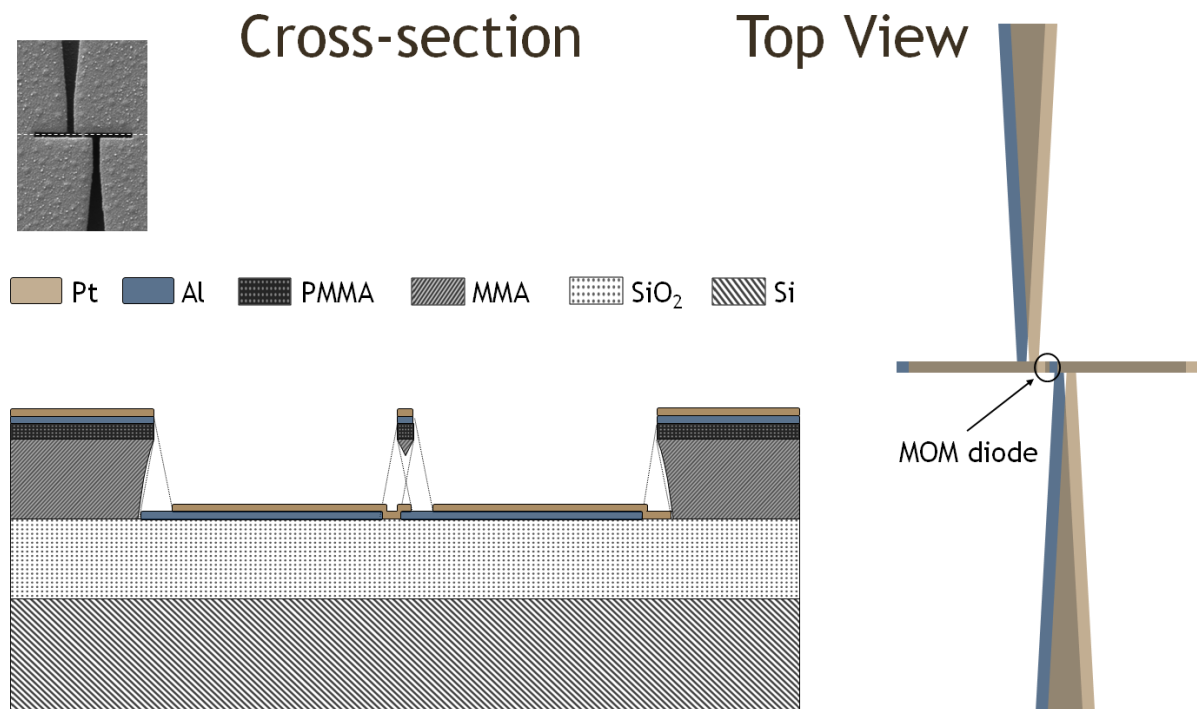 ensure that the ball in the tilt stage is flush with the extended tilt arm. Replace the standard substrate holder with the tilt stage. Be careful not to bump the tilt arm while connecting the tilt stage to the loading shaft. Close the lod and purge the load lock. When the pressure in the load lock is below 10^{-4} Torr, open the gate valve to the main chamber. Using the joystick on the power supply, make sure the vertical position of the substrate holder is 40. At this position, the substrate holder should be about 1" above the substrate shutter. Be sure to shutter the main chamber prior to the deposition.

Select aluminum on the gun 2 rail. On crystal monitor 2, select film 8 for aluminum (tooling factor=250, material density=2.70 gm·cm^{-3}, acoustic impedance=8.17×10^5 gm·cm^{-2}·s^{-1}). Turn on the power supply using the key. Press on-reset-on and ramp up voltage slowly to -10 kV. Turn on e-beam gun 2 and set mode to manual. Begin by turning the current knob to 20, wait one minute, and then turn the knob to 30. At around 35, the e-beam spot should be visible on the aluminum crucible. At this time, center the beam on the crucible. Slowly raise the current until the rate is between 2-4 Å·s^{-1}. For aluminum, do not exceed 40 mA current. When the rate is stable, open the substrate shutter and hit start on the crystal monitor controller. Since the tooling factor for aluminum is accurate, put down 300 Å for 30 nm.

When the aluminum deposition is complete, shut down the entire system, including the high voltage and e-gun. Wait approximately 5 minutes for the substrate to cool down. During this time, change the angle of the tilt stage. To do this, bring the tilt stage back through the load lock and trigger the loading arm by pressing it against the wall of the load lock.

Following the cool down, turn on the top KRI auto controller (mass flow controller). Select gas 3 (O_2) and set the value to 100. Press enable to start flowing O_2 into the chamber. Close the gate to the turbo pumps by turning the big wheel clockwise. Close the gate to the load lock pump by turning the black knob behind the load lock chamber. Monitor the pressure in the chamber using the digital display adjacent to the load lock chamber. Once the pressure approaches the desired value, reduce the mass flow controller to approximately 10. At this time, stabilize the pressure by altering the mass flow controller and load lock gate if necessary. After 30 minutes of oxidation, turn off the mass flow controller and shut the N_2 on the LCD screen. Reopen both the load lock and the turbo pump gates.

As mentioned, a controlled, low-pressure oxidation allows more precise control over the barrier thickness. Figure 49 shows the AlO_x thickness as a function of exposure time for an oxidation pressure of 10 µTorr. At three minutes, the mass flow control is switched on and gas begins to flow into the chamber. After about fifteen minutes, the oxide reaches a final thickness around 6 Å. The maximum oxide thickness is dependent on the oxidation pressure. In practice, it can vary from 6 Å for 10 µTorr oxidation pressure to 25 Å at atmospheric pressure. Following the results from a recent study detailing the device nonlinearity as a function of oxidation pressure, we choose oxidation pressures between 50 and 100 mTorr to produce diodes with dc resistances on the order of 100 kΩ [15].
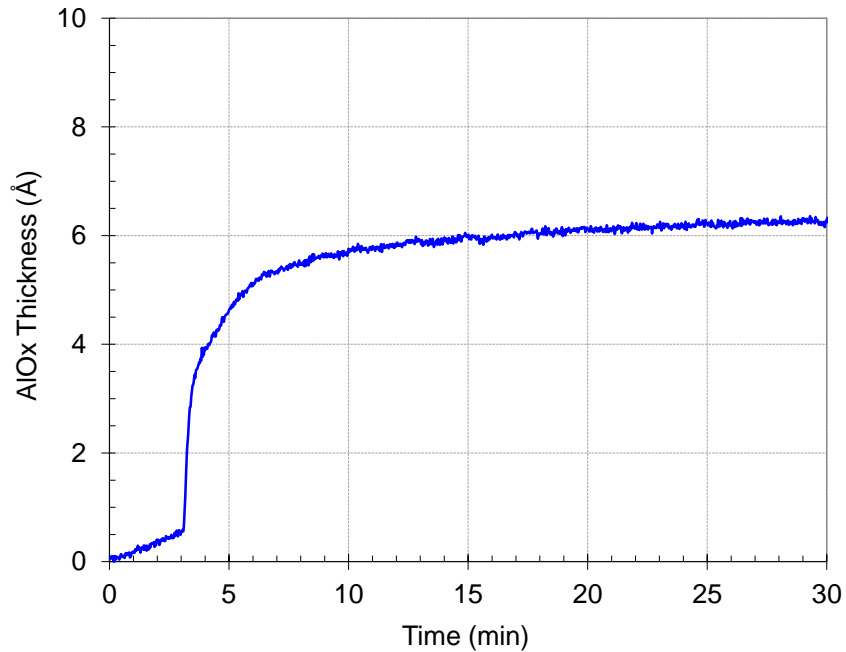
Figure 49: Oxide thickness as a function of exposure time for an oxidation pressure of 10 µTorr.

Select film 4 (platinum) on crystal monitor 2. Set the tooling factor=250, material density=21.4 gm·cm^{-3}, acoustic impedance=36.04×10^5 gm·cm^{-2}·s^{-1}. As before, turn the high voltage to -10 kV and turn on e-beam gun 2. Ramp up the current to around 80 mA, or until the e-beam becomes visible on the crucible. Center the beam and then ramp up the current to approximately 160 mA to obtain a rate around 2 Å·s^{-1}. To prevent resist reflow due to radiant heat, we break the platinum deposition into two 100 Å steps (this yields a total thickness of 30 nm). Between deposition, wait approximately 5 minutes for the substrate to cool. After the platinum deposition, bring the tilt stage back into the load lock, close the load lock gate and purge. Remove the devices carefully from the tilt stage. Be sure to always wear a grounding bracelet. For lift-off, use a methlylene chloride bath for approximately 5-10 minutes.

APPENDIX B: SIMULATION OF ANTENNA-COUPLED MOM DIODES

Numerical simulations are performed in Ansys High Frequency Structure Simulator (HFSS), a commercial electromagnetic finite element solver. HFSS is a finite element method solver. Solutions are generated by discretizing the model and solving for the electromagnetic fields everywhere in the solution volume. After each iteration, the mesh is refined at locations where the fields are highly concentrated and the difference between the fields from the current solution and those of the previous run is evaluated. Once this difference is below a specified threshold (typically 5 %), the solution is said to converge. The full antenna structure is modeled in HFSS, including the Al-Pt overlap from the shadow evaporation and the intermediate aluminum-oxide barrier. Both are shown in Figure 50.
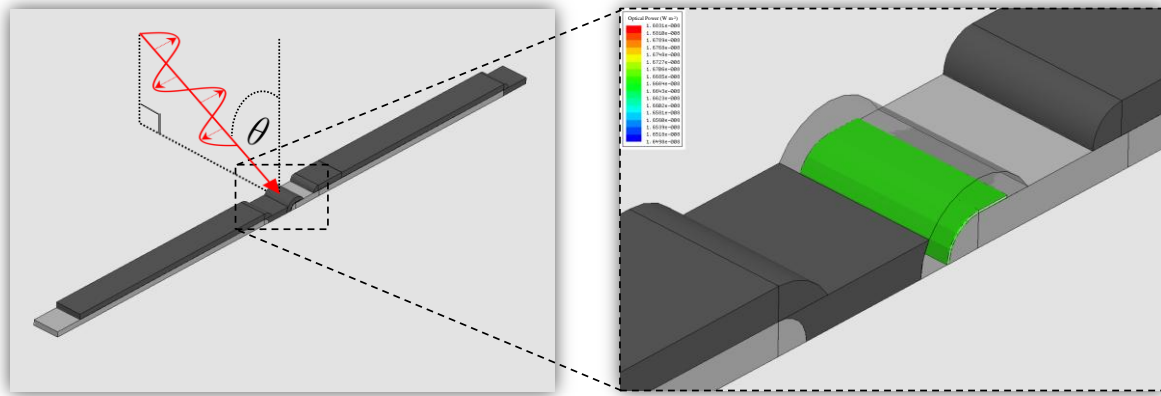
Figure 50: HFSS model of the antenna-coupled MOM diode. Inset image shows the aluminum-platinum overlap and the aluminum oxide barrier (green). The angle θ is measured in the plane perpendicular to the dipole (H-plane).

For the phased-array devices, the substrate consists of a ground plane and thin BCB layer. The model is generated by first drawing the antenna, substrate, and air boxes. Next, the bottom side of the BCB layer is assigned a perfectly conducting boundary condition. To do this, one selects the bottom face (Figure 51), right clicks and selects assign boundary, perfect E. All other external faces in the model are assigned radiation boundaries as shown in Figure 52. It is

imperative that all radiation boundaries are separated by at least one-quarter wavelength from any radiating elements.

Figure 51: Assigning perfectly conducting boundary conditions in HFSS.

Figure 52: Assigning radiation boundaries in HFSS.

From Eq. (9), a quantity proportional to the rectified current is computed as the power dissipated in the aluminum-oxide volume. The power dissipated represents the amo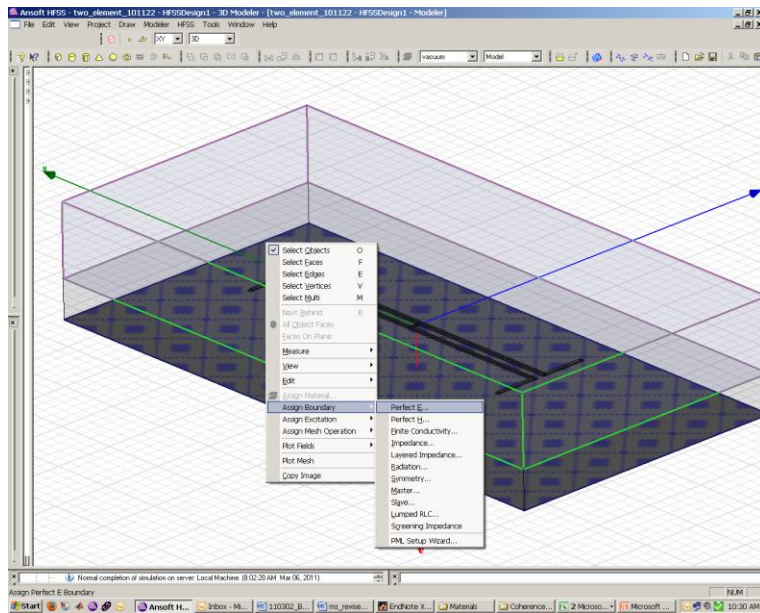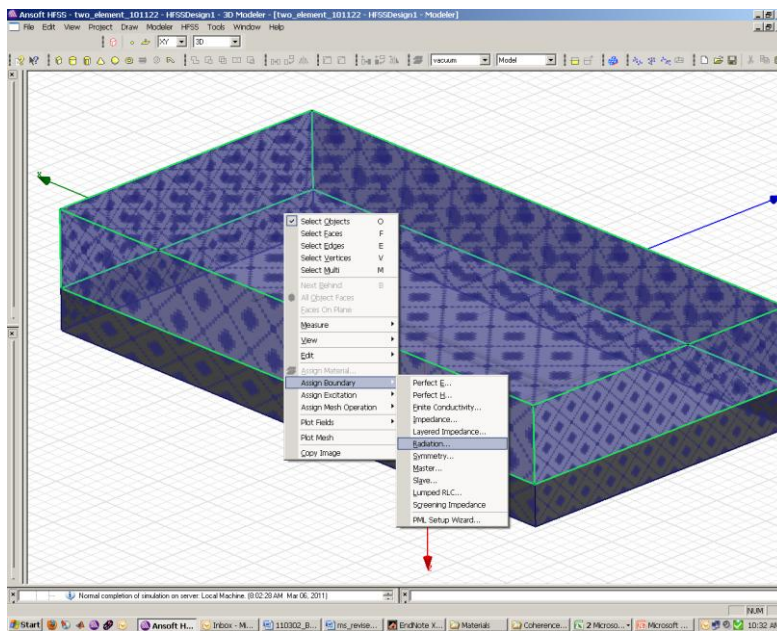unt of electromagnetic energy that is converted to thermal energy in the oxide. For a system with lossless dielectrics and perfect conductors, this quantity is equal to the time averaged optical power flow into the volume through the boundary surface. Although the rectified current will in general depend on the nonlinear resistance of the diode, the nonlinearity is negligible for typical IR test voltages ($\sim$10 µV at focus). To set up this calculation in HFSS, go to "HFSS" in the menu toolbar, select "Fields", "Calculator". Under the named expressions field, scroll down and select "Volume_Loss_Density". Once selected, click "Copy to stack". Click the "geometry" tab at the bottom left of the window, select "volume", locate the object that represents the diode or bolometer in the model, and then click "OK". Now, under the scalar column, click the integral sign. Click "Add" to input this quantity into the Named Expressions field. Name the quantity, e.g., "power_dissipated". If this is all done correctly, the window should resemble Figure 53.
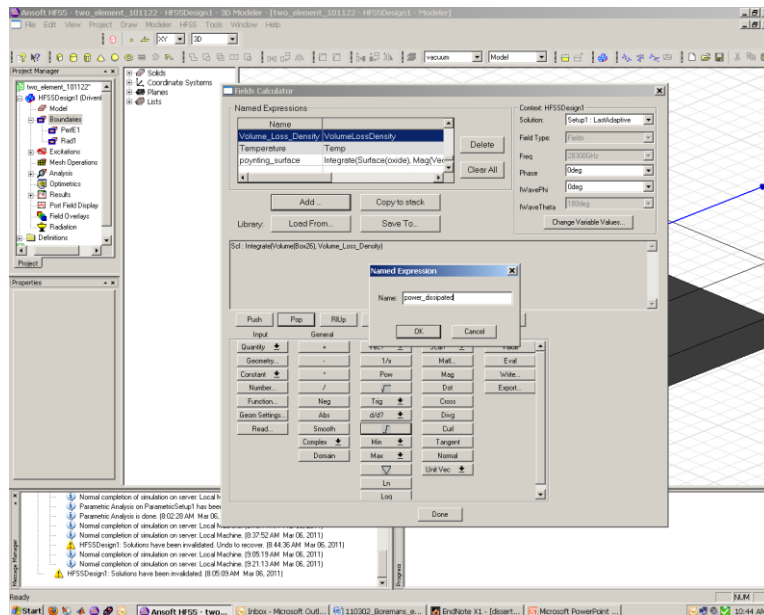
Figure 53: Fields calculator in HFSS.

To simulate the *F*/8 measurement configuration, the antenna is excited in HFSS with a Gaussian beam of waist w_0 = 115 μm with wavelength 10.6 μm (28.3 THz). To do this, right click "Excitations", select "Assign", "Incident Wave", "Gaussian beam". Select the preferred coordinate system and set the polarization and beam radius at focus. A radiation pattern is generated by computing the power dissipated in the oxide volume for each angle of incidence [41]. The material properties, including refractive index and thickness, are measured using a J.A. Woollam Infrared Variable-Angle Spectroscopic Ellipsometer (IR-VASE) and subsequently incorporated into the numerical models to increase the accuracy of the simulations [16].

To set up a report, right click "Results", "Create Fields Report", "Rectangular Plot". The quantity "power_dissipated" should appear in the calculator expressions category. Select the horizontal axis quantity under the "Families" section of the report window.

LIST OF REFERENCES

1. E. L. Dereniak and G. D. Boreman, *Infrared Detectors and Systems* (Wiley, New York, 1996).

2. P. M. Krenz, B. A. Lail, and G. Boreman, "Calibration of lead-line response contribution in measured radiation patterns of infrared dipole arrays," IEEE J. Sel. Top. Quantum Electron. **17**, 218-221 (2011).

3. S. Y. Yang, T. Izawa, and T. K. Gustafson, "Coupling characteristics of thin-film metal-oxide-metal diodes at 10.6 μm," Appl. Phys. Lett. **27**, 481-483 (1975).

4. M. Abdel-Rahman, F. Gonzalez, and G. Boreman, "Antenna-coupled metal-oxide-metal diodes for dual-band detection at 92.5 GHz and 28 THz," Electron. Lett **40**, 116 (2004).

5. J. A. Bean, B. Tiwari, G. H. Bernstein, P. Fay, and W. Porod, "Thermal infrared detection using dipole antenna-coupled metal-oxide-metal diodes," J. Vac. Sci. Technol. B **27**, 11-14 (2009).

6. J. G. Simmons, "Electric tunnel effect between dissimilar electrodes separated by a thin insulating film," J. Appl. Phys. **34**, 2581-2590 (1963).

7. I. Codreanu, F. Gonzalez, and G. Boreman, "Detection mechanisms in microstrip antenna-coupled infrared detectors," Infrared Phys. Technol. **44**, 155-163 (2003).

8. C. A. Balanis, *Antenna Theory: Analysis and Design,* 2nd ed. (Wiley, New York, 1997).

9. A. Sanchez, J. C. F. Davis, K. C. Liu, and A. Javan, "The MOM tunneling diode: theoretical estimate of its performance at microwave and infrared frequencies," J. Appl. Phys. **49**, 5270-5277 (1978).

10.   J. Wen, S. Romanov, and U. Peschel, "Excitation of gap plasmonic waveguides by nanoantennas," Opt. Express **17**, 5925-5932 (2009).

11.   S. M. Faris, B. Fan, and T. K. Gustafson, "Electronic tunneling currents at optical frequencies," Appl. Phys. Lett. **27**, 629-631 (1975).

12.   R. Stratton, "Volt-current characteristics for tunneling through insulating films," J. Phys. Chem. Solids **23**, 1177-1190 (1962).

13.   J. Bean, B. Tiwari, G. Szakmany, G. Bernstein, P. Fay, and W. Porod, "Antenna length and polarization response of antenna-coupled MOM diode infrared detectors," Infrared Phys. Technol. **53**, 182-185 (2010).

14.   J. Bean, B. Tiwari, G. H. Bernstein, P. Fay, and W. Porod, "Long-wave infrared detection using dipole antenna-coupled metal-oxide-metal diodes," in *Silicon Nanoelectronics Workshop, 2008. SNW 2008. IEEE,* (Honolulu, HI 2008), pp. 1-2.

15.   J. Bean, A. Weeks, and G. Boreman, "Performance optimization of antenna-coupled Al/AlO$_x$/Pt tunnel diode infrared detectors," IEEE J. Quantum Electron. **47**, 126-135 (2011).

16.   J. Ginn, B. Lail, D. Shelton, J. Tharp, W. Folks, and G. Boreman, "Characterizing infrared frequency selective surfaces on dispersive media," ACES Journal **22**, 184-188 (2007).

17.   P. M. Krenz, B. Slovick, J. Bean, and G. Boreman, "Alignment procedure for radiation pattern measurements of antenna-coupled infrared detectors," Opt. Eng. **49**, 033607 (2010).

18.   B. A. Lail, C. T. Middlebrook, P. M. Krenz, and G. D. Boreman, "Infrared dipole-coupled bolometer response on a hemispherical silicon immersion lens," Infrared Phys. Technol. **52**, 89-96 (2009).

19.   C. T. Middlebrook, P. M. Krenz, B. A. Lail, and G. D. Boreman, "Infrared phased-array antenna," Microw. Opt. Techn. Let. **50**, 719-723 (2008).

20.   D. B. Rutledge and M. S. Muha, "Imaging antenna arrays," IEEE Trans. Antennas Propag. **30**, 535-540 (1982).

21.   C. R. Brewitt-Taylor, D. J. Gunton, and H. D. Rees, "Planar antennas on a dielectric surface," Electron. Lett. **17**, 729-731 (1981).

22.   L. Martinu, O. Zabeida, A. Amassian, S. Larouche, C. Lavigne, J. E. K. Sapieha, D. E. Morton, and F. Zimone, "Plasma deposition of anti-reflective coatings on spherical lenses," in *Optical Interference Coatings,* (OSA Technical Digest Series (Optical Society of America, 2001), Banff, Canada, 2001).

23.   H. M. Presby and C. A. Edwards, "Near 100% efficient fibre microlenses," Electron. Lett **28**, 582-584 (1992).

24.   D. Z. Rogers, "Ball Lenses for coupling and collimation," Lightwave **16**, 104-110 (1999).

25.   M. A. George and D. Z. Rogers, "LPCVD of optical interference coatings for micro-optical applications," in *43rd Ann. Tech. Conf., Society of Vacuum Coaters*, 2000), 193-196.

26.   E. Y. M. Lee, N. H. Tran, and R. N. Lamb, "Growth of ZnS films by chemical vapor deposition of $Zn[S_2CN(CH_3)_2]_2$ precursor," Appl. Surf. Sci. **241**, 493-496 (2005).

27.   M. Ohring, *The Materials Science of Thin Films* (Academic Press, 1992).

28. C. T. Middlebrook, G. Zummo, and G. D. Boreman, "Direct-write electron-beam lithography of an IR antenna-coupled microbolometer onto the surface of a hemispherical lens," J. Vac. Sci. Technol. B **24**, 2566-2569 (2006).

29. B. L. Coleman, "Propagation of electromagnetic disturbances along a thin wire in a horizontally stratified medium," Philos. Mag. **41**, 276 (1950).

30. B. Slovick, P. Krenz, G. Zummo, and G. Boreman, "Evaporation of uniform antireflection coatings on hemispherical lenses to enhance infrared antenna gain," Infrared Phys. Technol. **53**, 89-93 (2010).

31. J. Bean, B. Slovick, and G. Boreman, "Influence of substrate configuration on the angular response pattern of infrared antennas," Opt. Express **18**, 21705-21713 (2010).

32. E. Hecht, *Optics,* 4th ed. (Addison-Wesley, Reading, Mass., 2002).

33. I. Codreanu and G. D. Boreman, "Influence of dielectric substrate on the responsivity of microstrip dipole-antenna-coupled infrared microbolometers," Appl. Opt. **41**, 1835-1840 (2002).

34. F. Gonzalez and G. Boreman, "Comparison of dipole, bowtie, spiral and log-periodic IR antennas," Infrared Phys. Technol. **46**, 418-428 (2005).

35. P. Krenz, R. Olman, B. Lail, M. Raschke, and G. Boreman, "Near-field measurement of infrared coplanar strip transmission line attenuation and propagation constants," Opt. Express **18**, 21678-21686 (2010).

36. A. W. Lee and Q. Hu, "Real-time, continuous-wave terahertz imaging by use of a microbolometer focal-plane array," Opt. Lett. **30**, 2563-2565 (2005).

37.   R. L. Olmon, P. M. Krenz, A. C. Jones, G. D. Boreman, and M. B. Raschke, "Near-field imaging of optical antenna modes in the mid-infrared," Opt. Express **16**, 20295-20305 (2008).

38.   W. H. V. Aulock, "Properties of Phased Arrays," Proceedings of the IRE **48**, 1715-1727 (1960).

39.   B. Slovick, J. Bean, and G. Boreman, "Angular resolution improvement of infrared phased-array antennas," IEEE Antenn. Wireless Propag. Lett., accepted (2011).

40.   T. A. Mandviwala, B. A. Lail, and G. D. Boremna, "Infrared-frequency coplanar striplines: design, fabrication, and measurements," Microw. Opt. Techn. Let. **47**, 17-20 (2005).

41.   B. Slovick, J. Bean, P. Krenz, and G. Boreman, "Directional control of infrared antenna-coupled tunnel diodes," Opt. Express **18**, 20960-20967 (2010).

42.   J. S. Huang, T. Feichtner, P. Biagioni, and B. Hecht, "Impedance matching and emissions properties of nanoantennas in an optical nanocircuit," Nano. Lett. **9**, 1897-1902 (2009).

43.   C. Fumeaux, M. A. Gritz, I. Codreanu, W. L. Schaich, F. J. González, and G. D. Boreman, "Measurement of the resonant lengths of infrared dipole antennas," Infrared Phys. Technol. **41**, 271-281 (2000).

44.   T. A. Mandviwala, B. A. Lail, and G. D. Boreman, "Characterization of microstrip transmission lines at IR frequencies - modeling, fabrication and measurements," Microw. Opt. Techn. Let. **50**, 1232-1237 (2008).

45.   J. W. Goodman, *Statistical Optics* (John Wiley & Sons, New York, 1985).

46. A. R. Thompson and J. M. Moran, *Interferometry and Synthesis in Radio Astronomy* (John Wiley & Sons, New York, 2001).

47. M. A. Johnson, A. L. Betz, and C. H. Townes, "10-μm heterodyne stellar interferometer," Phys. Rev. Lett. **33**, 1617-1620 (1974).

48. S. Brustlein, L. D. Rio, A. Tonello, L. Delage, and F. Reynaud, "Laboratory demonstration of an infrared-to-visible up-conversion interferometer for spatial coherence analysis," Phys. Rev. Lett. **100**, 153903 (2008).

49. C. Middlebrook, M. Roggemann, G. Boreman, N. Subotic, K. Cooper, W. Buller, W. Yang, and J. Alda, "Measurement of the mutual coherence function of an incoherent infrared field with a gold nano-wire dipole antenna array," Int. J. Infrared Milli. **29**, 179-187 (2008).

50. B. Slovick, J. Bean, L. Florence, G. Zummo, and G. Boreman, "Infrared antenna measurement of the spatial coherence function," Opt. Express, submitted (2011).

51. L. Mandel and E. Wolf, *Optical Coherence and Quantum Optics* (Cabridge Press, New York, 1995).

52. J. W. Goodman, *Introduction to Fourier Optics* (Roberts & Co., Englewood, CO, 2005).

53. M. A. Gritz, M. Metzler, M. Abdel-Rahman, B. Monacelli, G. Zummo, D. Malocha, and G. D. Boreman, "Characterization of a wavelength-tunable antenna-coupled infrared microbolometer," Opt. Eng. **44**, 036402-036405 (2005).

54. F. J. Gonzalez, B. Ilic, J. Alda, and G. D. Boreman, "Antenna-coupled infrared detectors for imaging applications," IEEE J. Sel. Topics Quantum Electron. **11**, 117-120 (2005).

55. D. Shelton, K. Coffey, and G. Boreman, "Experimental demonstration of tunable phase in a thermochromic infrared-reflectarray metamaterial," Opt. Express **18**, 1330-1335 (2010).